NOTE TO USERS

Low Temperature Magnetic Force Microscopy Studies of Superconducting Niobium Films

Mark A. Roseman
Centre for the Physics of Materials
Department of Physics, McGill University
Montréal, Canada
October 2001

A thesis submitted to the
Faculty of Graduate Studies and Research
in partial fulfillment of the requirements for the degree of
Doctor of Philosophy

Contents

List of Figures

List of Tables

Abstract

Low temperature magnetic force microscopy studies of superconducting niobium films have been undertaken with the goal of studying the interplay between artificial pinning centers and magnetic vortices.

Measurements were performed using a custom built low temperature magnetic force microscope, capable of operation at temperatures ranging from 4.2 K to room temperature. Special attention has been paid to optimizing the instrumentation through a detailed study of the noise characteristics, with particular emphasis placed on achieving a large signal-to-noise ratio and corresponding high force gradient sensitivity.

Magnetic force spectroscopy data has been used to deduce the critical temperature of the superconducting samples, based upon the repulsive Meissner interaction between the magnetic tip and the sample. Images of vortices as a function of applied magnetic field demonstrate the expected linear relation between vortex density and field strength, and confirms that only single vortices, each carrying one flux quantum, are observed. Two different methods are put forward to determine the magnetic penetration depth; one using magnetic force spectroscopy, the other using constant height imaging of vortices. Images of vortices as a function of temperature demonstrate that as temperatures rise, vortices become more easily depinned during the scanning process through interactions with the magnetic field of the tip. Dissipation images of vortices suggest eddy current damping as well as vortex motion within potential wells as major sources of energy loss. Studies on a patterned niobium film show that only interstitial vortices are easily detectable by MFM, but that a strong tip influence results in significant tip induced motion of these vortices around the antidots.

Résumé

Cette thèse a pour sujet l'étude de films supraconducteur de niobium, à l'aide d'un microscope à force magnétique à basse température (Low Temperature Magnetic Force Microscope, en anglais), et comme objectif l'étude des effets reliant les centres de fixation artificiels aux vortex magnétiques.

Un microscope à force magnétique spécialement conçu pour travailler à des températures pouvant aller de 4,2 K á 300 K, a été élaboré et construit. L'instrument a été minutieusement optimisé grâce à une étude détaillée des caractéristiques du bruit de fond. Une attention toute particulière a été portée á la maximisation du rapport signal à bruit ainsi qu'á sensibilité au gradiant de force.

La température critique de l'échantillon supraconducteur a été obtenue à l'aide de mesures de spectroscopie à force magnétique, en se basant sur l'intéraction répulsive de Meissner entre la pointe magnétique et l'échantillon. Les images de vortex en fonction du champ magnétique appliqué montrent bien une relation linéaire entre la densité des vortex et l'amplitude du champ. Ceci confirme également que chaque vortex observé ne contient qu'un seul flux quantique. Deux méthodes ont été mises de l'avant pour déterminer la profondeur de pénétration magnétique: l'une utilisant la spectroscopie à force magnétique, l'autre se basant sur l'étude des images de vortex en $\ll$ mode de hauteur constante $\gg$. Les images des vortex en fonction de la température montrent que, lorsque la température augmente, les vortex sont délocalisés par rapport aux centres de fixation artificiels lors de ballayages de la pointe. Ce phénomène est dû aux intéractions avec le champ magnétique de la pointe. Les images de dissipation des vortex suggèrent que les remous dans l'atténuation du courant, ainsi que les mouvements des vortex à l'intérieure des puits de potentiel, sont une source majeure de perte d'énergie. L'étude du film modelé de niobium montre que seul les vortex intersitiels sont facilement détectables avec un microscope à force magnétique à basse température, et que la pointe à une grande influence sur la mobilité des vortex autour des trous.

Acknowledgments

I would like to thank a number of people who have contributed to the development of this thesis and who have made my stay at McGill enjoyable and rewarding.

First I would like to thank my supervisor Dr. Peter Grütter for introducing me to the field of magnetic force microscopy. His patience and support have given me the freedom to explore this field, engage in some exciting research, make my own mistakes, and learn from them.

I am thankful to Dr. Dominic Ryan for his advice and guidance, and with whom I had the privilege of spending several weeks at TRIUMF. Dr. Zaven Altounian has also been a source of support for which I am grateful.

I am indebted to my colleagues Philip LeBlanc, Johan van Lierop, Xiaobin Zhu, Michel Godin, Vincent Tabard-Cossa, Alex Wlasenko, Ben Smith, Yan Sun, Manuel Pumarol, Yi-ting Huang, Valentin Yakimov and Robert Gagnon for their helpful discussions and assistance.

Special thanks to V. Metlushko and B. Ilic for providing me with excellent niobium samples.

Financial support through NSERC PGS B and FCAR B2 postgraduate scholarships is also greatly appreciated.

Finally, I would like to thank my parents and sister for their support and encouragement.

Statement of Originality

The author claims the following aspects of the thesis to be original contributions of knowledge.

- The design, construction and commissioning of a low temperature magnetic force microscope, capable of operation between 4.2 K and room temperature, in magnetic fields of up to 8 T. Special consideration has been given to modeling, characterizing and optimizing the various components of the system in order to minimize noise sources and achieve a high degree of force sensitivity.

  M. Roseman and P. Grütter, Rev. Sci. Instrum. **71**, 3782 (2000)

- Acquisition of magnetic force microscopy images of an unpatterned Nb film in various conditions of temperature and applied magnetic field, demonstrating the utility of MFM with regards to the study of magnetic vortices on superconducting samples. A method by which the magnetic penetration depth of the superconductor can be extracted from constant height MFM images of magnetic vortices is presented.

  M. Roseman and P. Grütter, submitted

- Magnetic force spectroscopy data acquired as a function of temperature is shown to be a viable technique by which the critical temperature T_c of a superconductor can be determined.

  M. Roseman and P. Grütter, submitted

- Demonstration of magnetic force microscopy imaging on a patterned superconductor, detailing tip-induced vortex motion around artificial pinning centers.

  M. Roseman, P. Grütter, A. Badía and V. Metlushko, J. Appl. Phys. **89**, 6787 (2001)

- Magnetic dissipation force microscopy images of magnetic vortices suggest eddy current damping as well as vortex motion within potential wells as major sources of energy loss.

  M. Roseman and P. Grütter, accepted Appl. Surf. Sci.

1

Introduction

Superconductors are materials which conduct electricity with no measurable resistance when cooled below a critical temperature T_c. This resistanceless conduction implies no energy dissipation (i.e. losses), a highly desirable feature from a technological point of view. For example, the replacement of copper wire found in existing electric generators with superconducting wire would increase efficiency up to an astonishing 99% [1]. Unfortunately, the requirement for refrigeration using liquid nitrogen and liquid helium currently restricts the applicability of superconductors to limited uses (the superconducting magnets in an MRI machine being a more common example). Researchers are continuously engaged in the development of new materials which exhibit superconductivity at increasingly higher temperatures, with the ultimate goal of one day producing a room temperature superconductor.

Besides temperature, the ability of a superconductor to carry electrical current is also governed by the behavior of magnetic "vortices", quantized structures which form in a periodic manner when magnetic field lines permeate the superconductor. Such fields are often created by the very current carried by the superconductor. Vortex motion, an effect resulting from the interaction between the vortices and the current in the superconductor, leads to energy dissipation, heating, and the eventual destruction of the superconducting state. Consequently, the understanding and control of vortex motion is currently a topic of great interest within the superconductivity community.

One means by which vortex motion may be suppressed is through the use of artificial pinning centers (APC's). These consist of a regular lattice of antidots patterned

into the superconducting material (in essence, holes in the superconducting material), which capture and pin vortices. Its efficacy may be ascribed in part to the commensurability between the antidot and vortex lattices, such that for various periodicities of the vortex lattice a majority of vortices are securely pinned within antidots. The success of this approach is demonstrated by bulk measurements such as magnetization and electrical resistivity, which show enhancements in the performance of the superconductor as vortex motion is suppressed by the APC's. However, the exact nature of the interaction between vortices and the pinning centers remains an open question, particularly so regarding the spatial arrangement and behaviour of so called "interstitial" vortices, those which reside in the spaces between antidots.

The task of probing magnetic structures (i.e. vortices) on a local scale, as opposed to bulk measurements which average over larger volumes, is one that lends itself well to the use of **Magnetic Force Microscopy** (MFM) [2,3]. A member of the scanning probe microscopy family, in this technique a sharp magnetically sensitive tip mounted on a compliant cantilever beam is brought into close proximity to a magnetic sample. Varying interactions between the magnetic field of the sample and the stray field of the tip lead to changes in the status of the cantilever. If these changes are recorded as a function of position while the tip is scanned relative to the sample, a three dimensional image of the magnetic structure of the sample is produced. If instead the magnetic interaction is recorded solely as a function of tip-sample separation as the tip is approached towards the surface, a force spectroscopy curve is generated.

The study of such superconducting systems by low temperature magnetic force microscopy is advantageous for several reasons, including a lateral resolution less than 100 nm; the ability to resolve both magnetic (vortices) and topographic (pinning centers) features of the sample, in order to better elucidate the interplay between the two; a relative insensitivity to surface conditions, requiring minimal sample preparation; and a limited ability to conduct time resolved imaging. A select number of groups have applied this technique towards the study of superconductors, including

one at the University of Basel [4], and one at the University of Texas [5], both working with high T_c superconductors, and a group at the Catholic University of Leuven [6] which studies Nb and $NbSe_2$ samples. The material presented in this thesis represents an advancement over previous work found in the literature, both in terms of the enhanced quality and signal-to-noise of the data, as well as in showcasing new experimental techniques such as magnetic force spectroscopy and dissipation imaging as applied to the study of magnetic vortices.

This thesis presents work conducted using a custom built low temperature magnetic force microscope. The instrument was designed, built and commissioned at McGill University, and was used in the study of vortices under various conditions of temperature and applied magnetic field, including both magnetic force imaging and magnetic force spectroscopy measurements. Samples consisted of two superconducting niobium (Nb) films; one of uniform thickness, the other patterned with artificial pinning centers. Initial work was conducted on the unpatterned Nb film, a test system used in order to develop the necessary experimental methods, gain experience with the technique, and demonstrate the utility of MFM towards the study of superconducting materials. Subsequent work on the patterned Nb film followed.

Niobium was chosen because of all the known superconducting materials, it is the most technologically important. It is utilized in a wide variety of applications, including superconducting solenoids, the windings of which are formed using NbTi, Nb_3Sn, or NbGe alloys; Josephson junctions, devices which consist of two layers of superconductor separated by a thin insulator, through which superconducting electrons tunnel; and even prototype superconducting transistor-like devices [7], which may one day replace the ubiquitous semiconductor-based transistor.

The structure of the thesis is as follows: Chapter 2 presents the design and a detailed characterization of the low temperature magnetic force microscope, with which all measurements were made. An overview of superconductivity is given in Chapter 3, to introduce some of the macroscopic properties and phenomenological

aspects of this unique phenomenon. We avoid a detailed discussion of the underlying microscopic mechanisms of superconductivity, as well as issues associated with unconventional high temperature superconductors, as these topics do not directly pertain to the data presented here and are beyond the scope of this work. Chapter 4 details the application of low temperature magnetic force microscopy towards the study of superconducting Nb films, including the imaging of vortices under various conditions of temperature and applied field, as well as a presentation of magnetic force spectroscopy data. A conclusion and outlook is presented in Chapter 5.

Throughout the thesis the unit Gauss (G) is used, where 10,000 G = 1 Tesla.

2

Magnetic Force Microscopy: Principles and Instrumentation

In this chapter the general concept of magnetic force microscopy is introduced. The design of the instrument is then presented, followed by a summary of its operating characteristics, a detailed analysis of the noise sources present in the system, as well as strategies followed in order to improve sensitivity by maximizing the signal-to-noise ratio. A condensed version of the material presented in this chapter can be found in [8].

2.1 Principles of Magnetic Force Microscopy

Magnetic force microscopy (MFM) is a technique by which a real space, three dimensional image of the magnetic structure of a sample is generated. Similar to the atomic force microscope [9], in which the interaction between a sharp tip, mounted on a flexible cantilever beam, and a sample are recorded as a function of tip position, the MFM instead boasts a magnetically sensitive tip which interacts with the magnetic stray field emanating from the sample surface. As the MFM tip is raster scanned across the sample, changes in the cantilever status, such as the dc deflection or the shift in the resonance frequency, are mapped as a function of tip position relative to the sample. The concept is schematically illustrated in Fig. 2.1, while typical MFM images are shown in Fig. 2.2.

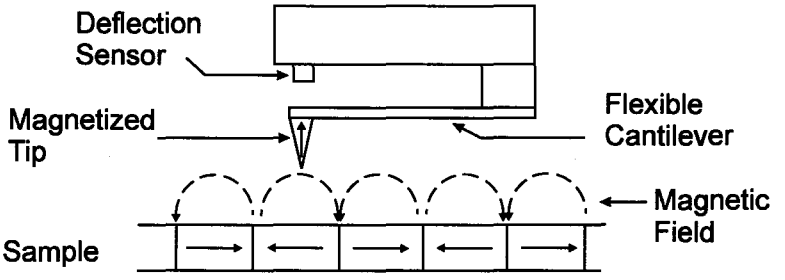

Figure 2.1: A magnetically sensitive cantilever interacts with the magnetic stray field of the sample. Resulting changes in the status of the cantilever are measured by the deflection sensor, and recorded to produce an image. Adapted from [3].

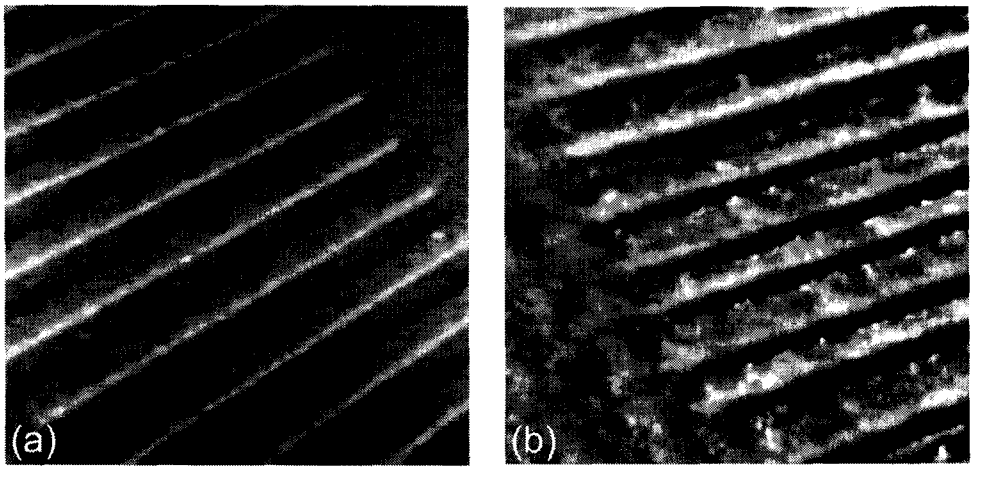

Figure 2.2: (a) 10×10 μm^2 area MFM image of magnetic tracks on a hard disk. (b) 30×30 μm^2 area MFM image of a floppy disk containing this thesis. The image has been differentiated in the x-direction in order to enhance contrast. The inferior quality of the magnetic transitions (i.e. reduced sharpness) of the floppy disk as compared with the hard disk emphasizes the disparity in material properties between the two, a reality reflected in their respective costs and storage densities.

2.1.1 Imaging Modes

Imaging may be performed in either static or dynamic mode. In the former, forces acting on the tip cause the cantilever beam to bend in response according to Hooke's law,

$$\Delta z = \frac{F_n}{k_{cb}} \tag{2.1}$$

where Δz is the deflection, F_n is the component of the force normal to the cantilever and k_{cb} is the spring constant of the cantilever.

This mode of operation is rarely employed in MFM, since an increase in sensitivity to long range forces, in particular long range magnetic forces, is achieved by operating the microscope in the dynamic mode [3]. In this case the cantilever is oscillated, typically at its resonance frequency, by a piezoelectric actuator, and can be treated as a one dimensional damped driven harmonic oscillator. This assumption holds for weak perturbations of the cantilever movement by tip-sample interactions, as is usually the case in dynamic force microscopy [10, 11].

The resulting equation of motion for the cantilever is given by [12]

$$m_{\text{eff}}\ddot{z}(t) + \beta_{\text{cb}}\dot{z}(t) + k_{cb}z(t) + F_{\text{t-s}}(\tilde{z}) = F_{\text{exc}}(t) \tag{2.2}$$

where z denotes the deflection of the cantilever, m_{eff} the effective mass, β_{cb} the damping coefficient of the cantilever motion, and k_{cb} the spring constant. The tip-sample interaction force denoted by $F_{\text{t-s}}$ is a function of the absolute tip-sample separation, $\tilde{z} = z + d$, where d is the cantilever support distance from the sample. The excitation of the cantilever via the piezoelectric actuator is described by F_{exc}.

For the case of small oscillation amplitudes A, such that A is much smaller than the decay length of the interaction between tip and sample, the assumption of a linear interaction force yields a simple analytic expression relating the interaction force to the measured frequency shift Δf [13],

$$\Delta f = \frac{f_0}{2k_{cb}}\frac{\partial F_{t-s}(z)}{\partial z} \quad \text{for} \quad \Delta f \ll f_0 \tag{2.3}$$

where f_0 is the cantilever resonance frequency in the absence of a tip-sample interaction. This expression generally holds for magnetic force microscopy applications, where the cantilever oscillation amplitude is typically less than 30 nm, while decay lengths may extend for hundreds of nanometers.

For the case of large oscillation amplitudes A much greater than the decay length of the measured interaction, the introduction of a nonlinear but conservative tip-sample interaction force gives [14]

$$\Delta f(d) = -\frac{1}{\sqrt{2}\pi}\frac{f_0}{k_{cb}A^{3/2}}\sum_{n=1}^{\infty}\frac{C_n I(n)}{(d-A/2)^{n-1/2}}, \tag{2.4}$$

with

$$I(n) = \begin{cases} \pi & n = 1 \\ \dfrac{\pi}{2^{n-1}}\displaystyle\prod_{i=2}^{n}\frac{2i-3}{i-1} & n > 1 \end{cases} \tag{2.5}$$

where the C_n are constants found from the Laurent series expansion

$$F_{t-s}(\tilde{z}) = \sum_{n=1}^{\infty}\frac{C_n}{\tilde{z}^n}. \tag{2.6}$$

A good review of the different methods relating resonance frequency shifts to tip-sample interactions can be found in [15].

2.2 Instrumentation

A block diagram of the principal components of the cryogenic magnetic force microscope is illustrated in Fig. 2.3. During imaging, the cantilever beam is oscillated at its resonance frequency, while the sample is raster scanned with respect to the cantilever using a piezo tube. A fiber optic interferometer serves as the deflection sensor for the cantilever, enabling a phase-locked loop (PLL) to measure its oscillation frequency. The PLL provides both a drive signal to continuously oscillate the cantilever, as well as a dc signal proportional to the measured cantilever resonance frequency. This dc

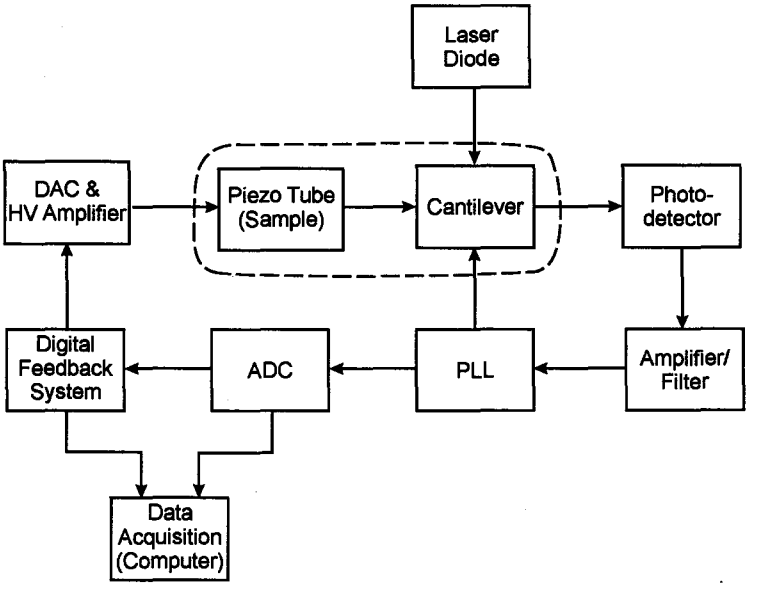

Figure 2.3: Block diagram detailing the components of the magnetic force microscope. The items enclosed within the dotted line are subjected to cryogenic temperatures.

signal is digitized and serves as a feedback signal, used to adjust the tip-sample separation in order to maintain a constant resonance frequency (and hence a constant tip-sample interaction), as set by the user.

The operation of the instrument at cryogenic temperatures necessitates the application of certain design criteria which distinguish it from similar room temperature systems. In order to operate at low temperatures, the microscope sits at the bottom of a superinsulated dewar, enclosed in a stainless steel vacuum can sealed using an indium o-ring (see Fig. 2.4). It is suspended from three thin-walled (0.020" thick) stainless steel tubes, which serve as feedthroughs for electrical connections, the optical fiber, and pumping lines for a turbomolecular vacuum pump. Cooling is achieved by immersing the vacuum can into the dewar, filled with either liquid nitrogen or liquid helium. A small volume ($\sim$1 cm^3) of helium exchange gas is introduced into the vacuum can to aid the cooling process, but is pumped out prior to imaging. The geometry of the microscope allows for its insertion into the 3" diameter bore

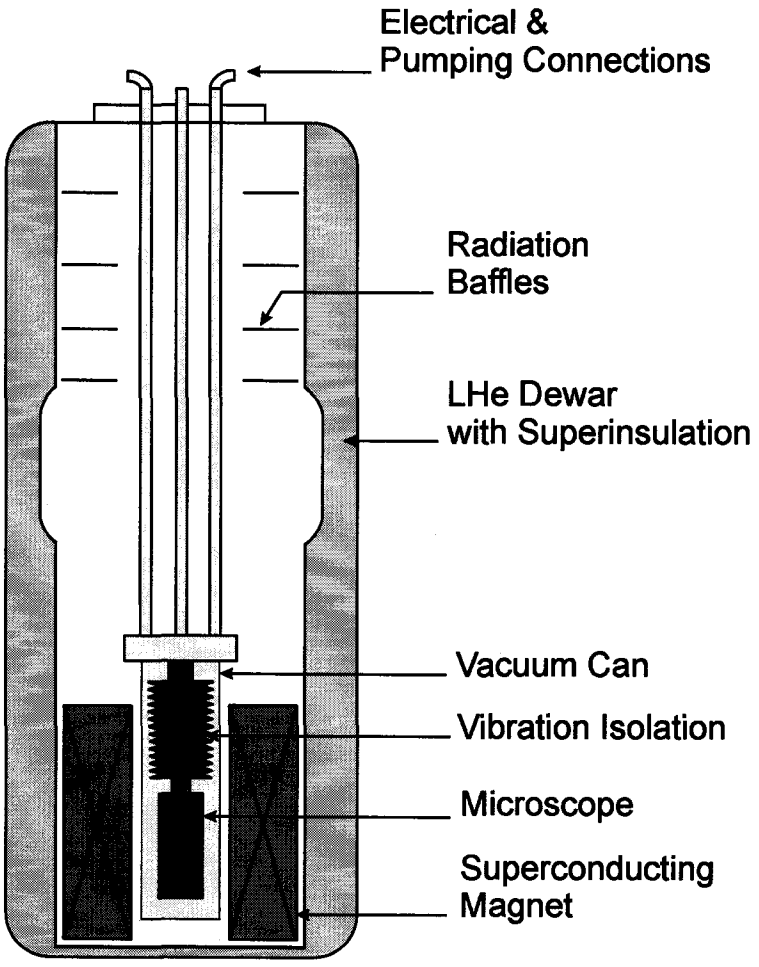

Figure 2.4: Illustration of microscope components within dewar.

of an 80 kG superconducting magnet, permitting the application of magnetic fields perpendicular to the sample surface.

The principal components of the microscope are illustrated in Fig. 2.5, and include electrical connections, vibration isolation, the sample positioner, thermometry apparatus, a flux gate magnetometer, the cantilever, the piezo tube, and the deflection sensor. These elements, as well as the associated data acquisition system, are discussed in the following sections.

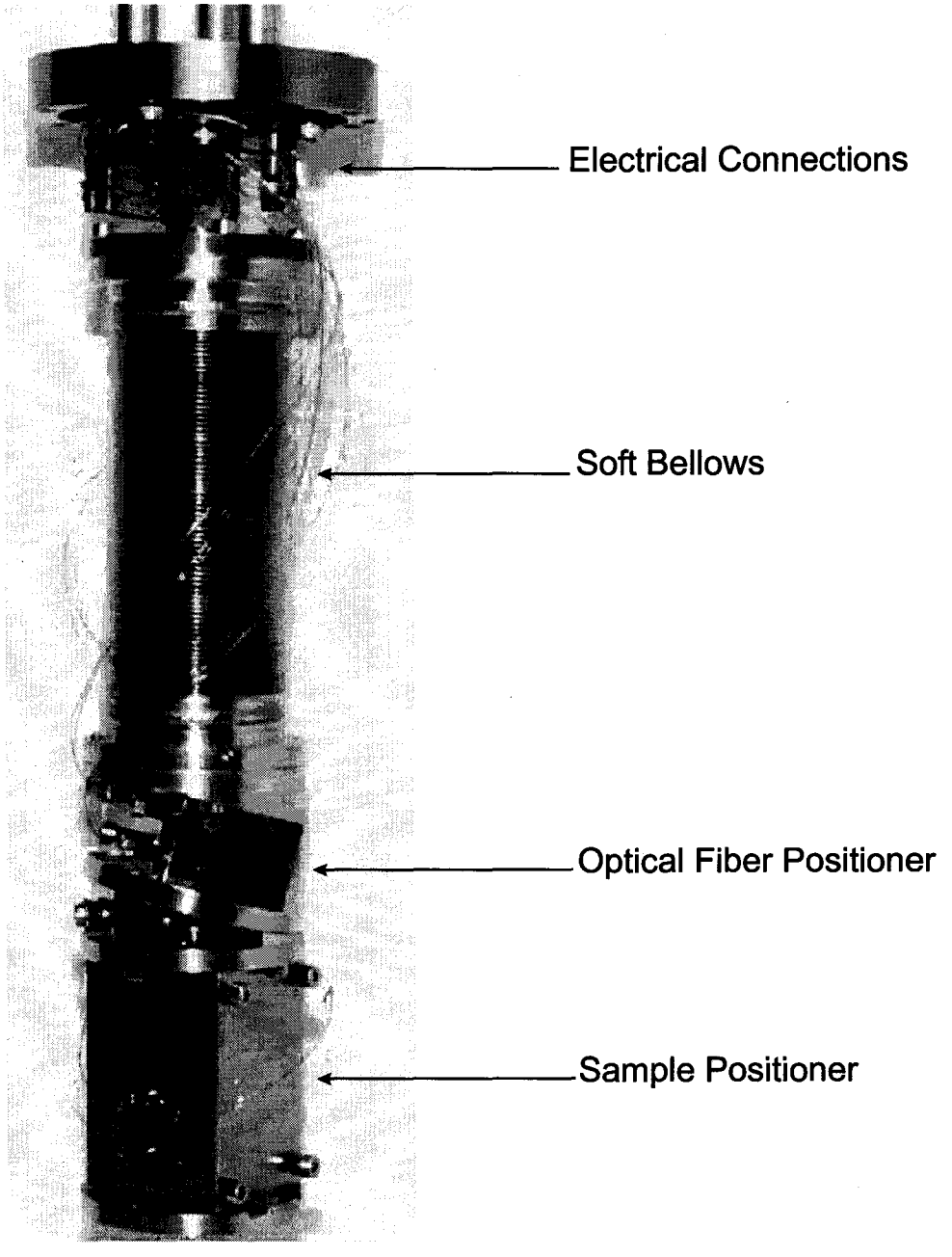

Figure 2.5: Photograph of the cryogenic magnetic force microscope, detailing its various components.

2.2.1 *Electrical Components*

All electrical connections from the top of the dewar to the microscope are made using Kapton coated copper and manganin twisted pair cables (0.005" diameter wire). In addition, there are two coaxial copper cables for especially sensitive measurements, one of which is routinely used in order to apply an electrostatic voltage to the sample during imaging. Cabling passes through the stainless steel tubes, and is clamped in a copper heat sink located at the top of the vacuum can. Modular contacts are made using Samtec [16] connectors, while permanent connections are made using silver epoxy [17].

2.2.2 *Vibration Isolation*

External vibrations such as those arising from building vibrations, pumps, the movement of people, and the boiling of liquid nitrogen or helium, can all contribute to unwanted motion of the cantilever. As measurements are based on the mechanical deflection of the cantilever, it is extremely important to effectively isolate and mechanically decouple the instrument from the surrounding environment. The reader is referred to [18] for a comprehensive review of the topic.

In the system, vibration isolation is achieved by securing the microscope beneath a soft, nested-type stainless steel bellows. Comprised of 70 convolutions, the bellows together with the microscope exhibits a vertical oscillation mode resonance frequency of about 4 Hz.[1]

In order to characterize the bellows and evaluate their effectiveness, seismometers [19] were used to measure the acceleration spectrum above and below the bellows. As illustrated in Fig. 2.6, accelerations resulting from external mechanical vibrations are attenuated by more than an order of magnitude over a 200 Hz bandwidth. Empirically it is found that the bellows effectively shields the microscope from various noise sources, including the boiling of liquid nitrogen/helium as well as vibrations from the

[1]Lower natural frequencies provide better vibration isolation [18].

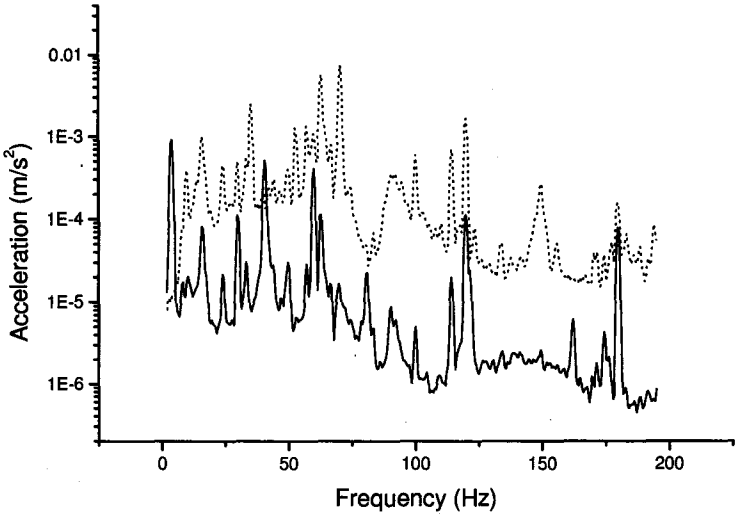

Figure 2.6: Acceleration spectrum of the nested bellows with the microscope suspended below, measured above (dotted line) and below (solid line) the bellows. Note the peak at 4 Hz on the solid line, corresponding to the vertical oscillation resonance of the bellows.

turbomolecular pump.

2.2.3 *In situ* Positioners

Before scanning, it is necessary to position both the sample and the deflection sensor (a fiber optic inteferometer, described in Section 2.2.8) close to the cantilever. Owing to the symmetric design of the instrument, lateral thermal drift of the optical fiber with respect to the cantilever is minimal.[1] Hence, no mechanism presently exists for *in situ* adjustment of the lateral position of the fiber, and consequently no provision is made for lateral realignment of the optical fiber once the cooling process has concluded. As well, no provision exists at this time for *in situ* course x–y (in-plane) motion of the sample. However, differential thermal contraction produces a relative motion in the z direction between the optical fiber, cantilever and sample. This ne-

[1]Empirically it was found that securing the fiber in the fiber chuck using Ecco Bond glue (Emerson & Cuming, Inc.) resulted in no observable drift of the optical fiber upon cooling. However, trials using Torr Seal (Varian Vacuum Products) yielded significant fiber movement.

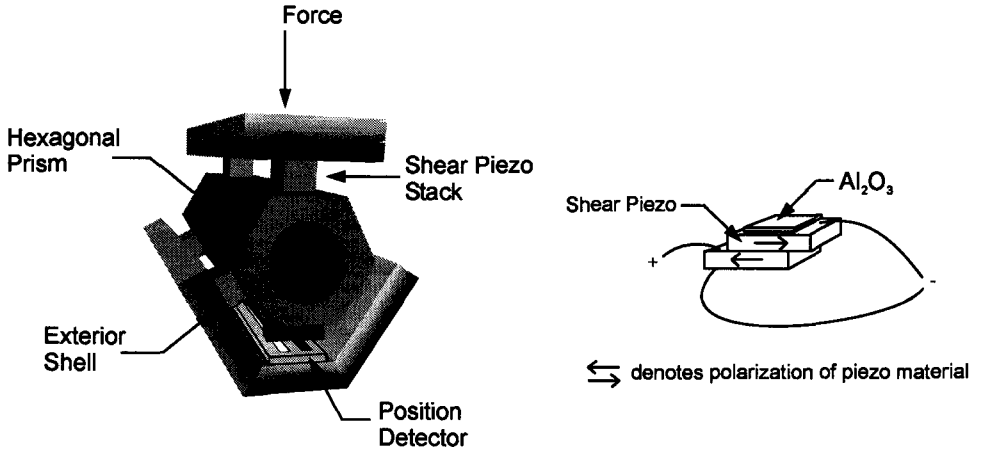

Figure 2.7: Illustration of the linear piezoelectric positioner. A hexagonal prism is held rigidly within an exterior shell (left). On the right is a detailed view of the shear piezo stack.

cessitates *in situ* adjustment of the cantilever-fiber and cantilever-sample separations at low temperatures, which are performed using two piezoelectric linear positioners.

Both the optical fiber positioner and the sample positioner are based on the same design [20], featuring a nonmagnetic stainless steel hexagonal prism clamped within an exterior shell. The clamping force is provided by four spring-loaded screws. Two stacks of shear piezos are located on each of three sides of the prism, with each stack comprised of two shear piezos glued one atop the other, capped with an aluminum oxide plate. These plates move against sapphire surfaces attached to the exterior shell. A schematic illustration of the positioner is shown in Fig. 2.7.

A sawtooth waveform of amplitude 200–800 V, at frequencies of 2–5 kHz, is applied to the piezos, producing a movement of the hexagonal prism with respect to the exterior shell in a slip-stick fashion. Step sizes of 10–20 nm for the optical fiber, measured using interferometric techniques, are routinely achieved at 4.2 K.

In order to verify the movement of the fiber-cantilever and sample-cantilever positioners during coarse approaches, and determine the approximate tip-sample separation prior to imaging, a position sensing device based on the design of a linear variable resistor is used. As illustrated in Fig. 2.8, a metallic brush is affixed to the

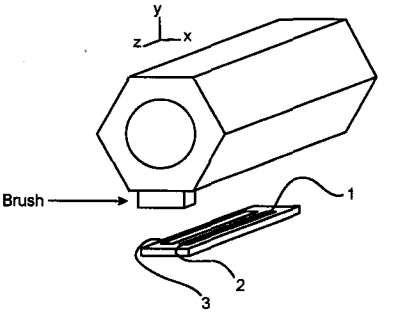

Figure 2.8: Illustration of the positioner detector system. A metallic brush on the underside of the hexagonal prism makes contact across two parallel strips, one a resistive carbon film (dark) and the other a low resistance path (light). The strip module is immobile and attached to the exterior shell. The ratio of the resistance between (1–3) to that between (1–2) gives the relative position of the brush along the length of the carbon film, as the hexagonal prism moves along the z direction.

underside of the central hexagonal prism of the positioner, and is in light contact with a resistive carbon film element located on the external shell. As the positioner is moved, the changing position of the brush alters the length of the current path through the carbon film, which is measured as a change in resistance; step sizes on the order of tens of nanometers are easily detectable. This allows for the determination of the proximity of the fiber and sample to the cantilever to within less than 1 μm.

2.2.4 Thermometry

For certain experiments, fine control over the sample temperature is extremely important. In order to measure and maintain a desired sample temperature while imaging, a Lake Shore Cryotronics 320 PID temperature controller system is used, along with a GaAlAs diode situated within a small copper mount upon which the sample is placed. The close proximity of the diode to the sample allows for accurate measurement and control of the sample temperature, which can be varied from 4.2–15 K when operating in a liquid helium environment, and between 77–100 K when operating in a liquid nitrogen environment.

2.2.5 *Superconducting Magnet and Flux Gate Magnetometer*

The superconducting magnet is an 80 kG Nb-Ti solenoid manufactured by American Magnetics, Inc. It is controlled using an AMI Model 412 Magnet Power Supply Programmer, which consists of a power supply programmer, a magnet voltage indicator, and a regulated current source for the magnet persistent switch heater. A magnet quench protection circuit is also incorporated into the unit, which in the event of a quench, quickly ramps the power supply output to zero. The programmer can be operated either manually or via computer. The power supply is an American Magnetics 1 kW, EMSII model 10-100. It uses a reverse biased heat sunk diode, rated for continuous operation at the full output current of the supply, in order to prevent a high voltage from being generated across the input terminals of the magnet in the event of a quench.

The amount of current required to generate a desired field is given by the field-to-current ratio, typically supplied by the magnet manufacturer, which for our system is 962 G/A. As currents approach zero however, superconducting magnets behave in a non-linear fashion and may no longer follow the linear relationship between field and current [21]. The work presented in this thesis required the application of small fields (see Chapter 4), with values ranging from several to tens of Gauss. In this small field regime, the field-to-current ratio becomes increasingly unreliable as a guide. In addition, no account is made for the presence of remanent fields originating from both the magnet and the microscope body, nor for the earth's magnetic field.

To address this, a home-built flux gate magnetometer is used in order to measure small fields (< 100 G in magnitude). The flux gate design is extremely advantageous, as it provides an absolute measure of the local field. It is located approximately 1 cm from the tip-sample interaction point, and provides a measure of the magnetic field to within less than 1 G.

Approximately 1 cm in diameter and 4 mm high, the magnetometer consists of an outer coil of approximately 1000 turns, within which two smaller coils (10 turns

each) are situated. All three coils are oriented in the same direction. A small piece of Allied Signal Metglass 2714AZ 0.65 mm material is located in the center of one of the inner coils.

During operation, a 2 kHz sine wave is applied to the outer coil, while the induced electromotive force (emf) of the inner coils is monitored. The two smaller coils are connected in series opposition, which cancels out the pick-up of the ac field. The magnetic field generated by the outer coil drives the magnetic material through saturation during each half cycle, producing a corresponding voltage peak on the induced emf. These peaks occur with a separation of T/2, where T is the period of the sine wave. The application of an external dc magnetic field effectively shifts the hysteresis curve of the magnetic material, altering the time interval between adjacent voltage peaks (see Fig. 2.9). A determination of the dc magnetic field strength can then be made either through a calibrated reading of the time separation between voltage peaks, or through the application of a known nulling field to reset the time separation between peaks.

2.2.6 *Piezo Tube*

To acquire an image, the sample is scanned with respect to the stationary cantilever using a piezo tube. The scan range of the tube is determined by its dimensions, material composition, operating temperature, as well as the applied voltage.

The 2" long piezo tube is made of EBL #3, and achieves a scan range of 40 μm at room temperature with applied voltages of $\pm$ 100 V.[1] Lower temperatures yield a reduced response from the piezo tube, producing scan ranges of 14 μm and 10 μm at 77 K and 4.2 K respectively, with similar applied voltages.

2.2.7 *Cantilevers*

Two types of cantilevers are commonly used in the system. Both are batch microfabricated and commercially available. The silicon nitride cantilevers, manufac-

[1]The depoling field of the piezo tube is 254 V_{rms}.

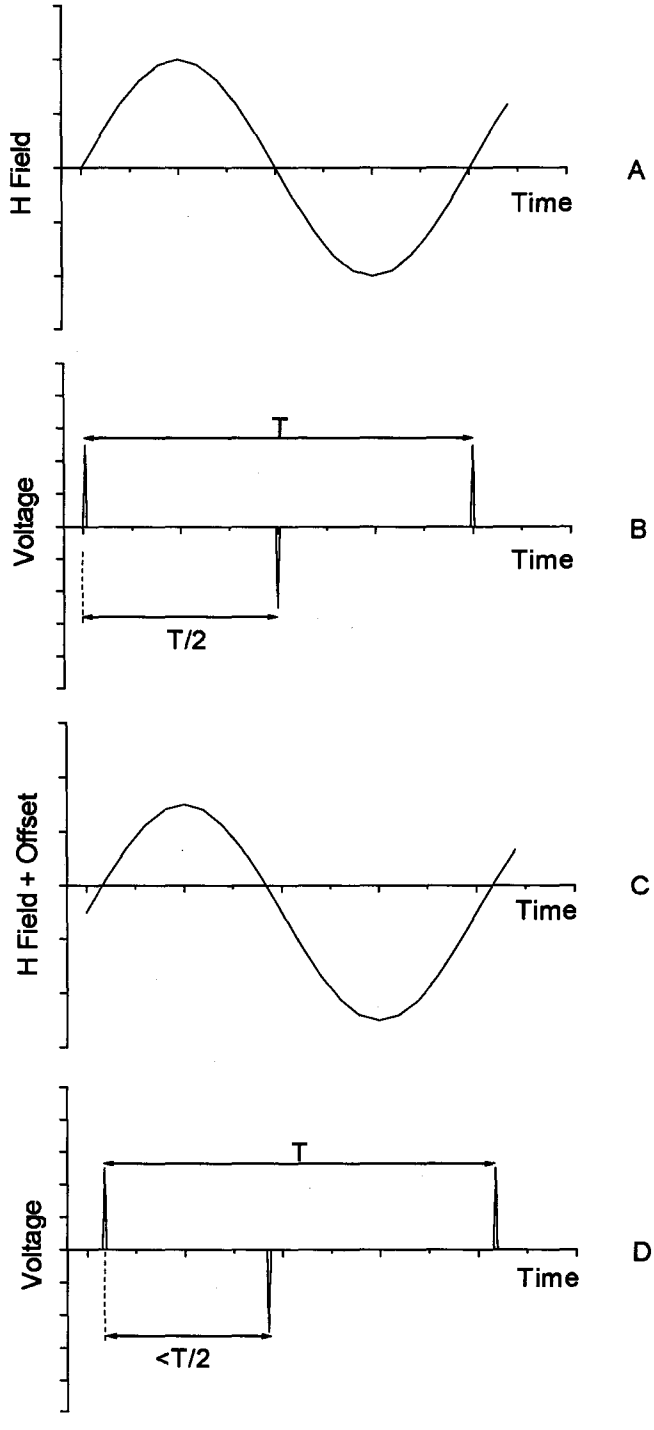

Figure 2.9: In A, the field acting on the magnetic material is shown as a function of time. The corresponding voltage peaks, the result of the induced emf during saturation, is shown in B. In C, an external dc magnetic field alters the total field acting on the magnetic material, effectively shifting the curve along the y-axis. This shift results in a change in time between adjacent peaks, as shown in D. Here, T is the period of the sine wave.

tured by ThermoMicroscopes [22], have nominal resonance frequencies of 30 kHz and spring constants of 0.1 N/m. The single crystal silicon cantilevers, manufactured by Nanosensors [23], have resonance frequencies of about 70 kHz and spring constants of about 1 N/m. In order to make the cantilevers magnetically sensitive, a cobalt coating, typically 10–40 nm in thickness, is evaporated onto one side of the tip, using shadowing to restrict the deposition of the film. The cantilever is then magnetized along the tip axis prior to installation in the microscope. As well, a thin layer of gold (typically 40 nm) is evaporated onto the back side of the silicon nitride cantilevers, in order to enhance its reflectivity to the laser light of the deflection sensor.

2.2.8 Deflection Sensor

A fiber-optic based interferometer system, first described in [24], is used to detect cantilever deflections and thereby measure the cantilever resonance frequency. This system was chosen over another common low temperature detection method, the piezoresistive cantilever [25–28], for several reasons. Firstly, the fiber optic interferometer is well suited for low temperature applications; only one end of the optical fiber need be subjected to cryogenic temperatures, with all other electrical and optical components of the detection system, including the laser diode and photodetector circuit, operating at room temperature. In addition, the interferometric technique provides for an absolute calibration of cantilever deflection using the laser wavelength as a reference, an advantageous feature for quantitative measurements. By contrast, piezoresistive cantilevers are less attractive, not only due to the limited range of available spring constants and resonance frequencies, but also over concerns regarding power dissipation (typically several mW [28], two orders of magnitude greater than in our system).

A schematic diagram of the interferometer is illustrated in Fig. 2.10. A Sharp LT023MS single transverse mode, multi-longitudinal mode[1] laser diode is used, op-

[1]The mode-hopping which is characteristic of multi-longitudinal mode lasers helps to prevent deleterious effects to the laser, so called "optical-feedback", which result when reflected photons returning

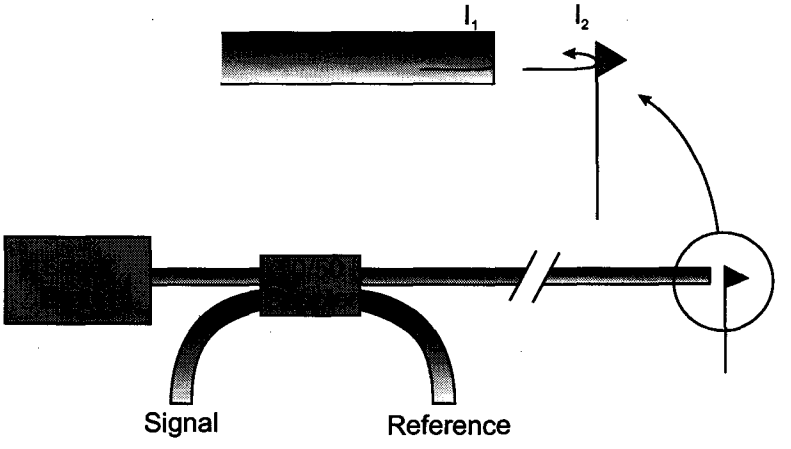

Figure 2.10: Components of the interferometer.

erating at a wavelength of 780 nm. The laser diode is driven with an ILX Lightwave LDX-3412 Precision Current Source with a stability of $\leq$50 ppm (10–30 min.) [30]. During routine operation, the laser diode typically emits between 150 μW to 200 μW of power, depending upon the driving current. The laser light is directed via an FC connector into a 50/50 bi-directional coupler,[1] which directs half of the light into the cryostat via 80 μm diameter 3M single mode fiber-optic cable (rated attenuation of 3.0 dB/km @ 820 nm), to serve as a deflection sensor for the cantilever beam. As shown in Fig. 2.11, 20–100 μW of laser power is emitted from this cleaved end of the optical fiber under normal operating conditions. The remaining light intensity may then be directed from the coupler to a photodiode in order to monitor fluctuations in output light intensity, although this option is not presently implemented in our system.

Owing to the cleave at the fiber end within the cryostat, approximately 4% of the light intensity is reflected back at the fiber/air (fiber/vacuum) interface. This beam I_1 interferes with the remaining light which exits the fiber, reflects off of the oscillating cantilever beam, and then re-enters the fiber as I_2. The intensity of the

along the optical fiber re-enter the laser cavity [29].

[1]Manufactured by Gould Fiber Optics

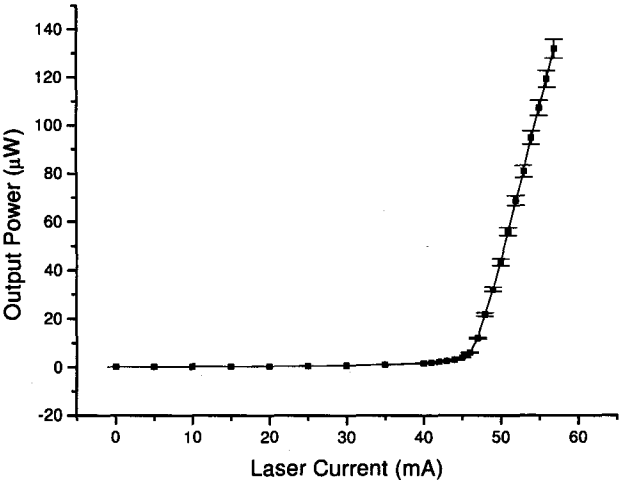

Figure 2.11: The laser light power emitted from the cleaved end of the optical fiber, as a function of laser diode driving current, measured using a Newport Model 815 Power Meter. Under typical operating conditions, the laser diode is driven by 52–55 mA of current.

resulting interference pattern I_T is given by

$$I_T = I_1 + I_2 + 2\sqrt{I_1 I_2}\cos\delta \tag{2.7}$$

where δ is the phase difference between beams I_1 and I_2, given by $\frac{4\pi z}{\lambda}$ where z is the cantilever-fiber separation and λ is the laser light wavelength. As the cantilever is oscillated, the cavity length defined by the cantilever-fiber separation is altered, resulting in a modulation of the observed intensity.

For optimal sensitivity to cantilever motion, the fiber-cantilever separation should correspond to $n\frac{\lambda}{8}$, where n is an odd integer. At this separation, $\partial I/\partial z$ is maximized and observed intensity changes are approximately linear for small cantilever oscillations. A typical fiber-cantilever arrangement for our system is shown in Fig. 2.12. Both the optical fiber and the cantilever are canted at an angle of 15° with respect to the sample surface, in order to restrict the magnetic interaction to the tip region of the cantilever, while still preserving the desired 90° orientation between fiber and cantilever.

Figure 2.12: Photograph of the cantilever beneath the optical fiber.

The optical interference signal is detected by a UDT Sensors PIN-020A photodiode, with an active area of 0.20 mm^2 and a responsivity η of approximately 0.5 A/W for the wavelength of light used [31]. The photodiode is reverse biased with 15 V in order to decrease its capacitance, thereby reducing its response time and increasing its bandwidth.[1] The signal current generated by the photodiode is converted to a voltage using a Burr Brown OPA 111 operational amplifier, which offers the lowest noise in the FET op-amp class [32]. A gain of 10^6 is achieved using a metal film resistor, which contributes less noise than a typical carbon composition resistor [33]. The complete circuit is illustrated in Fig. 2.13.

2.2.9 Phase-Locked Loop

The signal from the photodetector circuit is amplified and filtered by a 2-channel, 8 pole, 0.1 Hz to 200 kHz low pass/high pass filter.[2] It is then directed to a phase-locked

[1]Dark current noise generated when operating the photodiode in the photoconductive mode (application of reverse bias) is negligible in our system.

[2]Krone-Hite model 3382 Tunable Active Filter

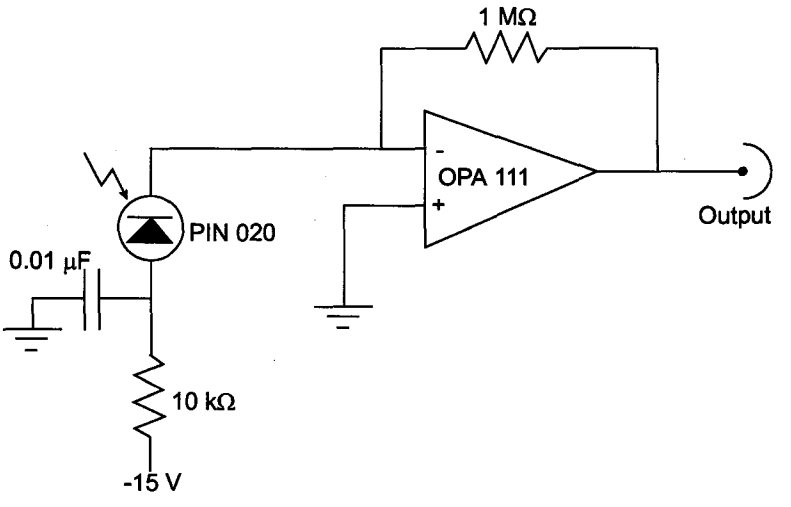

Figure 2.13: The light incident on the photodiode generates a current which is converted into a voltage using an operational amplifier.

loop (PLL), designed at IBM Zurich but assembled and commissioned at McGill University. Within a 10 kHz window centered on the resonance frequency, the PLL tracks the frequency of the cantilever by monitoring the phase relationship between the excitation signal (generated by the PLL) and the measured cantilever response (the PLL input). It thus ensures that the oscillation frequency is exactly at the peak of the resonance curve.

The PLL provides two output signals (in addition to the excitation signal directed to the cantilever). The first is a dc signal Δf, proportional to the cantilever resonance frequency (1 mV = 1 Hz), which is filtered and then digitized using a 16 bit analog-to-digital converter in order to serve as the feedback signal upon which constant force gradient images are acquired. The second signal is proportional to the excitation signal, and serves as a dissipation signal which is representative of the amount of energy required to continuously oscillate the cantilever at a constant, predetermined amplitude. This signal is used to detail local dissipation within a sample, a measure of non-conservative interactions between cantilever and sample, and forms the basis of Dissipation Force Microscopy [34,35]. A schematic illustration of the PLL is given

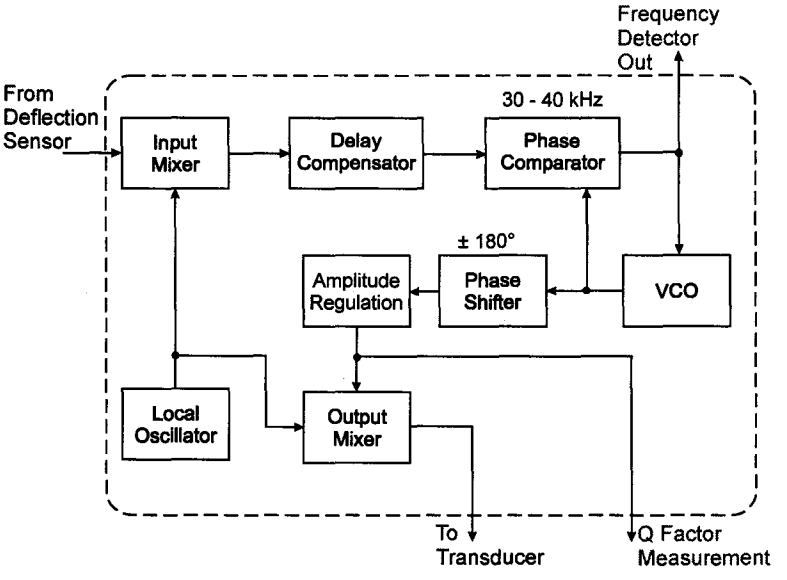

Figure 2.14: Block diagram representation of the phase-locked loop (PLL).

in Fig. 2.14; for a more complete description, see [36].

The operational bandwidth of the PLL is controlled by proportional and integral gain settings of the feedback loop of the voltage controlled oscillator (VCO). The proportional gain reduces the rise time between input and response, but will always have a steady-state error associated with it. The integral gain eliminates this steady-state error, but may make the transient response worse (since it acts somewhat like a low-pass filter). Larger settings of the proportional and integral gains lead to a quicker, yet noisier response. Smaller values of the gains produce smaller errors at the expense of measurement speed.

In order to characterize the bandwidth of the PLL, a test signal was substituted for the cantilever deflection signal. This sinusoidal signal was frequency modulated with a span of 100 Hz at a rate which varied from 10–300 Hz, while the output signal Δf was monitored. Since the system is set such that 1 mV = 1 Hz, the frequency modulation of the input signal by 100 Hz should yield an amplitude of the Δf signal of 100 mV peak to peak. Results are illustrated in Fig. 2.15, and show that the

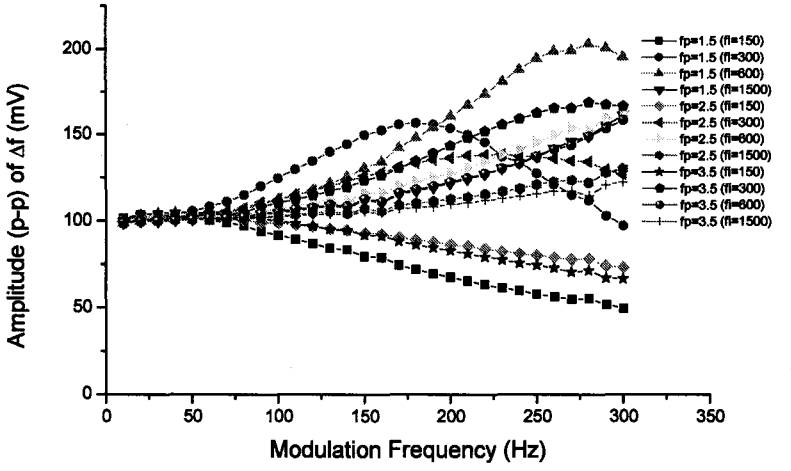

Figure 2.15: The amplitude (peak-to-peak) of the PLL output Δf, plotted as a function of the frequency modulation of the test signal. Each curve corresponds to different settings of the proportional (f_p) and integral (f_i) settings.

PLL response is heavily influenced by the gain settings of the VCO feedback loop. Consequently, values for these settings should be carefully chosen such that the PLL bandwidth is large enough to accommodate the scanning speed.

2.2.10 *Feedback and Control System*

The output of the PLL is digitized and then directed to a digital feedback unit, whereby it serves as the feedback signal upon which constant force gradient images are acquired. The control system and software are manufactured by East Coast Scientific, and run on a 486 based personal computer. The reader is referred to [37] for technical details regarding the feedback system and control software.

2.3 *Instrumentation Limits and Noise*

A thorough understanding and appreciation of the various noise sources in the measurement apparatus is important not only in the optimization of the equipment, but also serves as a guide for selecting suitable experiments. Specifically, it allows for an estimate of the minimum detectable frequency shift measurable, a quantity directly related to the smallest detectable force gradient (see Eq. 2.3).

The following analysis has been undertaken with the aim of determining the sensitivity of the microscope. Various noise sources have been identified and their contributions estimated. For simplicity, these contributions have been divided into two groups. First, those noise sources associated with the cantilever and deflection sensor electronics, including the laser diode, the photodetector circuit, and cantilever thermal motion are listed. The second category includes noise sources arising from the electronic feedback and control systems.

2.3.1 *Cantilever and Deflection Sensor Noise Sources*

Noise terms associated with the laser diode and cantilever include laser shot, intensity, phase and optical feedback noise, and the thermal motion of the cantilever. The photodetector circuit, which converts currents generated by the photodiode (both the signal and the aforementioned noise terms) into voltages, itself introduces two additional noise contributions [32]: Johnson noise, which is generated by the feedback resistor; and a "noise gain" term which results from the presence of the operational amplifier within the circuit.

A general discussion of noise sources applicable to force microscopy can be found in [11], while [38–40], provide more detailed information regarding laser diodes. The following lists individual noise contributions, then compares the theoretical and measured values for the system.

Laser Shot Noise

Laser shot noise results from the statistics of photons incident on the photodiode. Laser light striking the diode will generate a current i related to the incident optical power P by

$$i = \eta P \tag{2.8}$$

where η is the responsivity of the detector. The corresponding mean-squared current noise $\overline{i^2}$ is given by

$$\overline{i^2}_{Shot} = 2e\eta P \ [\mathrm{A}^2/\mathrm{Hz}] \tag{2.9}$$

where e is the electronic charge. When this mean-squared current noise passes through a resistor of value R, it generates a mean-squared voltage noise given by

$$\overline{v^2}_{Shot} = 2e\eta PR^2 \ [\mathrm{V}^2/\mathrm{Hz}] \tag{2.10}$$

Laser Intensity Noise

Sources of noise including mode-partition noise, mode-hopping noise, $1/f$ noise and spontaneous emission have complicated theories, but can often be grouped into a Laser Intensity Noise term [38, 39], given for a typical laser diode by

$$\overline{i^2}_{Intensity} = \eta^2 P^2 \times 10^{-13} \ [\mathrm{A}^2/\mathrm{Hz}] \tag{2.11}$$

$$\overline{v^2}_{Intensity} = \eta^2 P^2 R^2 \times 10^{-13} \ [\mathrm{V}^2/\mathrm{Hz}] \tag{2.12}$$

Laser Phase Noise

This term results from the finite coherence length of the laser, and depends on the optical path length difference of the interferometer (that is, the separation between the cleaved end of the optical fiber and the cantilever). The resulting mean-squared current noise is

$$\overline{i^2}_{Phase} = \eta^2 P^2 4\pi\Delta\nu\tau^2 \ [\mathrm{A}^2/\mathrm{Hz}] \tag{2.13}$$

while the corresponding mean-squared voltage noise is given by

$$\overline{v^2}_{Phase} = \eta^2 P^2 R^2 4\pi\Delta\nu\tau^2 \ [\mathrm{V}^2/\mathrm{Hz}] \tag{2.14}$$

where $\Delta\nu$ is the linewidth of the laser and τ is the optical path length difference of the interferometer, divided by the speed of light.

Thermal Cantilever Motion

The presence of a cantilever in the system contributes an additional noise term resulting from its thermal motion. Treating the cantilever as an isolated one-dimensional harmonic oscillator, the expressions for the noise current and noise voltage are given by

$$\overline{i^2}_{Cantilever} = \left(\frac{4\pi\eta P}{\lambda}\right)^2 \frac{4k_B T}{\omega_0 k_{cb}} \frac{Q}{Q^2(1-\frac{\omega^2}{\omega_0{}^2}) + \frac{\omega^2}{\omega_0{}^2}} \ [\mathrm{A}^2/\mathrm{Hz}] \tag{2.15}$$

$$\overline{v^2}_{Cantilever} = \left(\frac{4\pi\eta PR}{\lambda}\right)^2 \frac{4k_BT}{\omega_0 k_{cb}} \frac{Q}{Q^2(1-\frac{\omega^2}{\omega_0{}^2})+\frac{\omega^2}{\omega_0{}^2}} \text{ [V}^2\text{/Hz]} \tag{2.16}$$

where k_B is Boltzmann's constant, T is the absolute temperature, λ is the laser wavelength, ω_0 is the resonance frequency of the cantilever, and k_{cb} is the spring constant of the cantilever.

Johnson Noise

Johnson noise [41], named after the scientist at Bell Laboratories who first studied it in 1928, results from the thermal interaction between the free electrons and vibrating ions in the load resistor R of the photodetector circuit. This process gives rise to a noise current and noise voltage [42] given by

$$\overline{i^2}_{Johnson} = \frac{4k_BT}{R} \text{ [A}^2\text{/Hz]} \tag{2.17}$$

$$\overline{v^2}_{Johnson} = 4k_BTR \text{ [V}^2\text{/Hz]} \tag{2.18}$$

where k_B is Boltzmann's constant, T is the absolute temperature, and R is the value of the resistor. This noise term exhibits a constant density over all frequencies, and appears directly at the output of the circuit without amplification.

Operational Amplifier Noise

The noise arising from the presence of the operational amplifier is frequency dependent, and begins to rise at a frequency f_i determined by the feedback resistor R, diode capacitance C_D, and the differential input capacitance and common-mode input capacitance of the operational amplifier C_{OPA} [43]. It then levels off at a frequency determined by the stray capacitance present in the circuit C_S, and is finally rolled off by the operational amplifier bandwidth limit. This "noise gain" is illustrated in the Bode plot of Fig. 2.16.

Our system uses a feedback resistor R = 1MΩ. With a 15 V bias applied to the photodiode, the diode capacitance $C_D \approx 4$ pF [31]. The additional capacitance C_{OPA} contributed by the operational amplifier is approximately 4 pF [43].

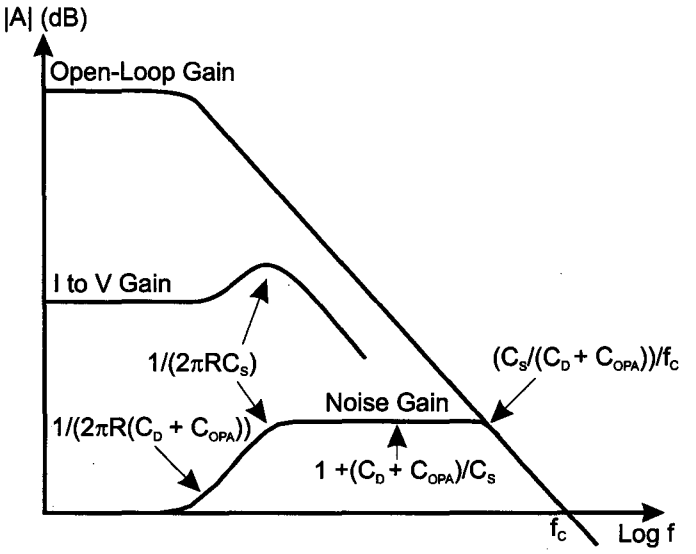

Figure 2.16: The Bode plot illustrates the response of the OPA 111 based circuit, in particular the noise gain, current to voltage gain and open-loop gain characteristics. The cut-off frequency f_c of the OPA-111 is 2MHz.

The measured response of the photodiode with no light incident on the detector is illustrated in Fig. 2.17. A polynomial fit to the graph yields a dc value of 129 $\pm$2nVrms/$\sqrt{\text{Hz}}$, in excellent agreement with the expected Johnson noise value of 128 nVrms/$\sqrt{\text{Hz}}$. The expected frequency $f_i = 19,900$ Hz as well as the general shape of the curve are also in good agreement with the illustration of Fig. 2.16.

Current to Voltage Gain

As illustrated in Fig. 2.16, the current to voltage (I to V) gain of the cantilever deflection signal is not flat over all frequencies. Rather, it exhibits a 3 dB peak followed by a roll off caused by stray capacitance [43]. The observed amplitudes of the deflection signal, as well as the noise contributions from Section 2.3.1, are thus amplified at the output, according to the current to voltage gain profile of the circuit.

The current to voltage gain characteristics of our system were measured using an LED light source, coupled into the fiber optical cable via an FC connector. A sine wave applied by a function generator was used to drive the LED at frequencies ranging from 1 kHz to 200 kHz. The resulting output signal amplitude of the photodetector

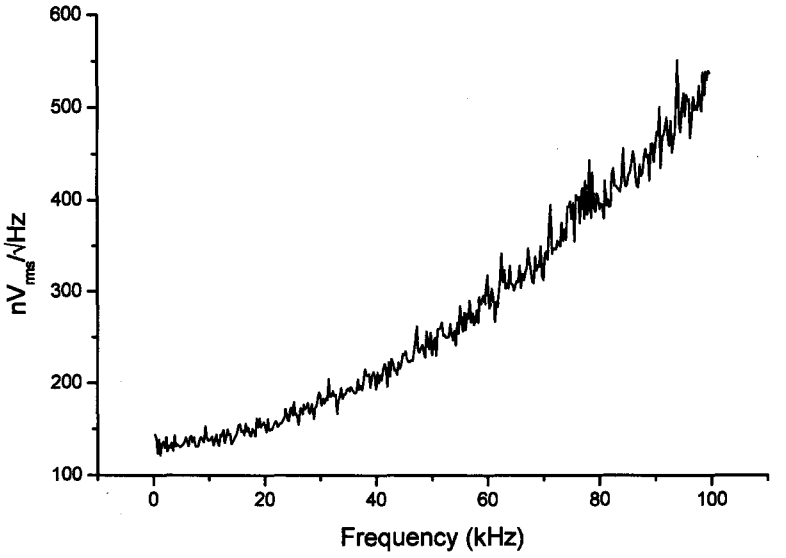

Figure 2.17: The response of the photodetector circuit as a function of frequency with no incident light upon the detector. The frequency dependent noise arising from the operational amplifier is evident. The 100 kHz bandwidth of the plot is set by the limits of the spectrum analyzer used in the measurement.

circuit was measured using an oscilloscope, and is shown in Fig. 2.18.

Total Noise Contribution

The total noise contribution from the cantilever, deflection sensor and photodetector circuit can be summed according to Fig. 2.19, given that noise voltages, or currents, which are independently generated are uncorrelated, and hence may be added by taking the square root of the sum of the squares of the individual terms (that is, mean-squared values can be added) [33]. Laser shot noise, laser intensity noise, laser phase noise and thermal cantilever motion are thus added, then scaled according to the current to voltage gain curve of the system. Operational amplifier noise and Johnson noise are then added at the output.

A sample calculation is shown in Fig. 2.20, which illustrates the experimentally measured and simulated power spectral density for the case of a silicon nitride cantilever at a temperature of 5 K. The corresponding values of contributing noise terms are listed in Table 2.1. The cantilever has a resonance frequency $f = 30,781$ Hz, a

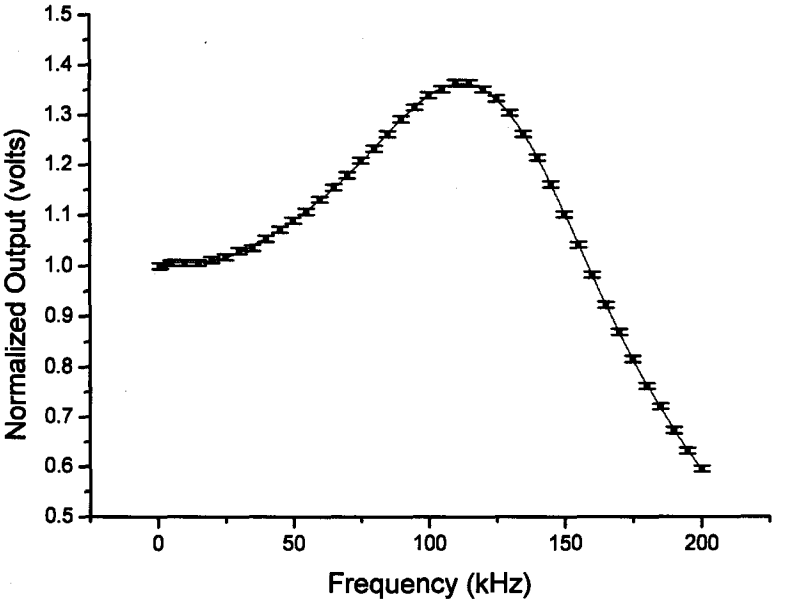

Figure 2.18: The response of the photodetector circuit as a function of frequency when illuminated by an LED. Note the 3 dB peak (approximately 1.4 times the DC value) at around 110 kHz just before the roll-off.

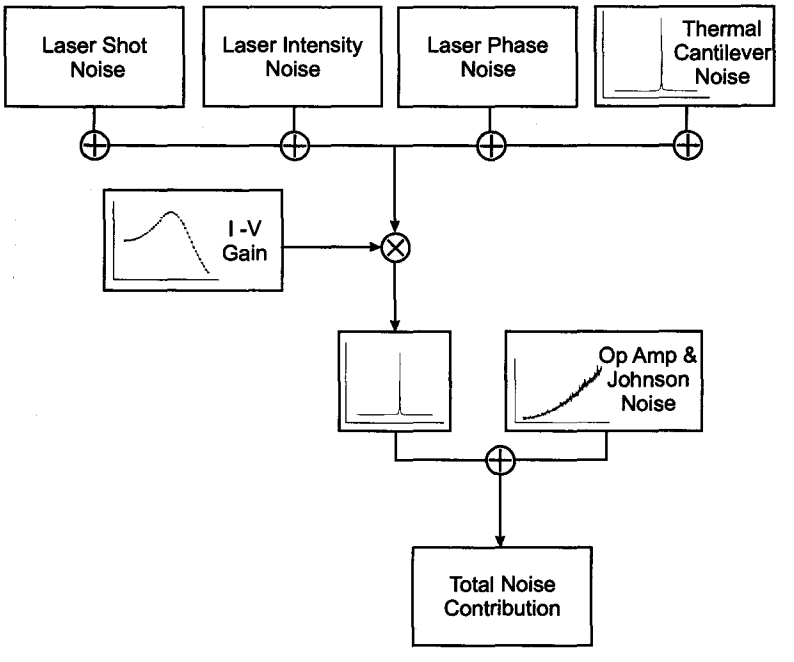

Figure 2.19: Block diagram representation of the addition of laser diode, photodiode and photodetector circuit noise sources.

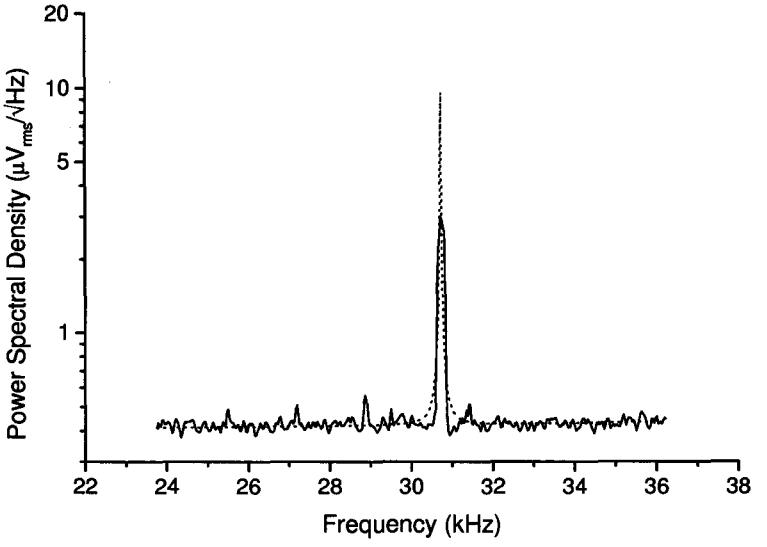

Figure 2.20: The power spectral density of a silicon nitride cantilever at 5 K (solid line), along with the theoretical noise value (dotted line).

quality factor $Q = 11,843$, and a nominal spring constant $k_{cb} = 0.1$ N/m. It was positioned far from the sample in order to avoid any anharmonicity due to tip-sample interactions, and the excitation piezo was grounded (that is, the cantilever was not driven). The calculated and measured power spectral density plots show good agreement, especially at frequencies off resonance. The discrepancy between peak shapes of the two curves can be attributed to the windowing function (a Blackman-Harris window) of the Stanford Research Systems SRS FFT network analyzer used for the measurement, which affects the binning process and hence influences the peak height and shape. However, the integrated areas under the two curves differ by less than 10%.

At frequencies off resonance, the largest contribution arises from shot noise of the interferometer, whereas thermal effects dominate near and at the resonance frequency. During imaging, the cantilever is driven at its resonance frequency with an amplitude comparable to several $\mathrm{mV}/\sqrt{\mathrm{Hz}}$, orders of magnitude greater than the thermal noise contribution at this frequency. However, shot noise contributions remain unaffected by cantilever oscillation amplitude, and are frequency independent.

Shot Noise	7.8×10^{-14} V^2/Hz
Laser Phase Noise	5.5×10^{-14} V^2/Hz
Resistor Johnson Noise	1.7×10^{-14} V^2/Hz
Laser Intensity Noise	6.0×10^{-15} V^2/Hz
Thermal Cantilever Noise off resonance	1.9×10^{-17} V^2/Hz
Thermal Cantilever Noise on resonance	8.8×10^{-11} V^2/Hz

Table 2.1: Calculated values of contributing noise terms for the case of a silicon nitride cantilever at 5 K.

2.3.2 *Electronic feedback and Control Systems Noise*

The second category includes bit noise from analog-to-digital or digital-to-analog converters, electrical cross talk between signals, as well as intrinsic limitations within the electronic feedback and control systems.

To characterize this effect, we tested the PLL and data acquisition system by acquiring data as during a normal scan, except that instead of the deflection signal, the PLL input consisted of a high signal-to-noise ratio (>108 dB), constant frequency (70 kHz) test signal generated by an FFT Network Analyzer. Ideally, the resulting "scan" should record the same frequency value for each of the 256 by 128 pixels of the "image", since the input signal was of constant frequency and high spectral purity (< -70 dBc). An example of a histogram of the pixel values of such an "image" is illustrated in Fig. 2.21. A Gaussian fit to the distribution and the determination of the standard deviation σ, gives a conservative estimate on the frequency resolution, which we have chosen as 2σ. Under these test conditions, we found the frequency resolution of the electronic feedback and control system components to be 0.20 ± 0.01 Hz in a 72 Hz bandwidth. While this resolution is larger than DSP based systems currently available, which currently boast frequency resolutions on the order of 5 mHz, it is not in fact the limiting factor with regards to the sensitivity of the microscope, as discussed in the following section.

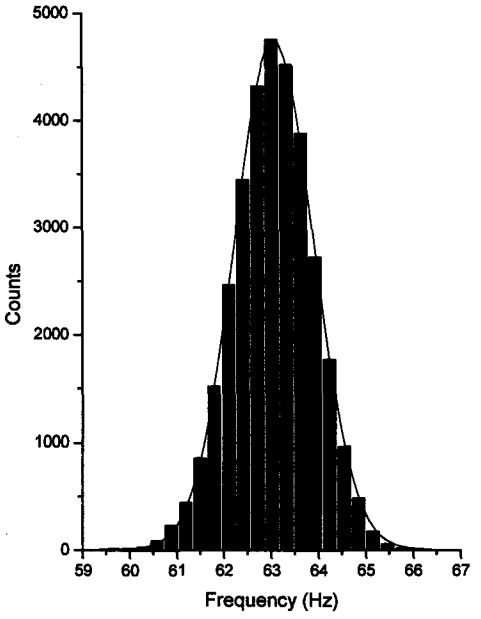

Figure 2.21: This histogram has a standard deviation σ of 0.836 ± 0.005 Hz. The frequency resolution would then be 2σ, or 1.67 Hz. The mean is arbitrary.

2.3.3 *Sensitivity of the Microscope*

The power spectral density of a thermally oscillated cantilever illustrated in Fig. 2.20 featured both a thermal peak as well as background noise. The presence of noise at frequencies off resonance is extremely relevant when determining the system frequency resolution, a fact often overlooked within the AFM/MFM community. This is because the PLL measures the frequency of the cantilever deflection signal over a nonzero bandwidth, including both the cantilever resonance peak (signal) as well as a background (noise).

For the case of an ideal PLL, capable of determining the frequency of an input signal to an arbitrary precision, the resolution will be limited by the quality of the input signal (assuming the local oscillator exhibits superior spectral purity, as is often the case). The smallest measurable frequency change δf_{signal}, will depend on both the anharmonic contributions and finite width of the signal, as well as the background noise; features characterized by the signal-to-noise ratio of the input

signal [35,36]. This can easily be seen by considering the PLL as a "frequency meter", which measures the frequency of an input signal by measuring the time between a fixed number of zero crossings of the sinusoidal input signal. The precision of the zero crossing measurement and thus the achievable frequency resolution is determined by the noise inherent in the signal, which tends to broaden the zero crossings and hence introduce uncertainty in the time measurement.

In reality, the PLL exhibits an intrinsic limit δf_{PLL}, indicative of the ultimate frequency resolution possible given an ideal input signal. The effective system frequency resolution of the acquired data is determined either by the finite signal-to-noise ratio of the input signal, or by the intrinsic limit of the PLL. For a well designed system, $\delta f_{\mathrm{PLL}} < \delta f_{\mathrm{signal}}$.

In order to determine the sensitivity of the complete system under temperature and pressure conditions consistent with imaging at liquid helium temperatures, we performed a similar procedure as used in Section 2.3.2. However, in this case the cantilever deflection signal was used instead of a test signal.

With the cantilever driven by the PLL, as is the case during scanning, but positioned far from the sample so as to avoid any anharmonicity due to tip-sample interactions, a test image was acquired. Again, the x and y scan generators were disabled, so as to prevent motion of the tip relative to the sample. In this case a frequency resolution of 0.60 ± 0.02 Hz in a 72 Hz bandwidth was recorded, for a silicon nitride cantilever with a resonance frequency $f = 30,781$ Hz and a quality factor $Q = 11,843$, at 5 K. Using Eq. 2.3, with $k_{cb} = 0.1$ N/m the nominal spring constant value, a frequency resolution $\delta f = 0.60$ Hz corresponds to a measurable force gradient resolution of approximately 3.9×10^{-6} N/m.

Given that the electronic and control systems exhibited a smaller frequency resolution under test conditions ($\delta f = 0.20$ Hz), this suggests that the quality of the deflection signal limits the sensitivity of the system. Since shot noise contributes the largest background noise term to the deflection signal, we infer that the system is

therefore limited by the shot noise of the interferometer. The best way to enhance the frequency resolution of the system then is to increase the optical power incident on the photodiode. This improves the signal-to-noise ratio as the square root of the optical power, since the signal increases linearly with optical power, while the shot noise increases only as the square root. Operating the laser diode at a larger drive current is one possible solution. However, this also results in several deleterious effects, including increased heating of the cantilever, greater susceptibility to optical feedback owing to changes in the mode spectrum of the laser diode at higher output power, as well as a shortening of the laser diode lifetime.

3

Overview of Superconductivity

In this chapter a brief introduction and overview of superconductivity is given, which provides sufficient background necessary to understand and interpret results presented in Chapter 4. For a general introduction to superconductivity, the reader is referred to [44]. A more advanced treatment of the subject can be found in [45].

3.1 The Discovery of Superconductivity

Superconductivity was first discovered in 1911 by the Dutch physicist, Heike Kamerlingh Onnes [46], three years after having liquefied helium. While studying the temperature dependence of the electrical resistance of mercury, he noted that once cooled below about 4 K, the resistance of the sample dropped suddenly to zero and remained unmeasurable at lower temperatures. This result was in stark contrast to the expected behavior, where the resistance would decrease when cooled below room temperature, falling linearly down to about one third of the Debye temperature of the material, after which it drops less rapidly. Recognizing that the sample had undergone a transition into a new state characterized by zero electrical resistance, Onnes christened the phenomenon "superconductivity".

3.2 The Critical Temperature T_c

The temperature at which a superconductor loses its electrical resistance is called the superconducting transition or critical temperature, T_c. Table 3.1 lists the transition

Element	T_c (K)
Aluminum	1.175 ± 0.002
Indium	3.408 ± 0.001
Lead	7.196 ± 0.006
Mercury	4.154 ± 0.001
Niobium	9.25 ± 0.02
Tin	3.722 ± 0.001
Titanium	0.40 ± 0.04
Tungsten	0.0154 ± 0.0005
Zinc	0.850 ± 0.01

Table 3.1: Critical temperatures of selected superconducting elements [47].

temperatures for some metallic elements. Alloys and metallic compounds typically exhibit higher transition temperatures than those of the metallic elements. Recently, the discovery of superconductivity in magnesium diboride (MgB_2) with $T_c \approx 39$ K has generated a great deal of excitement [48], as its transition temperature is nearly a factor of 2 greater than previously known superconducting metallic compounds (e.g. Nb_3Ge has a transition temperature of 23 K). Some high T_c ceramic oxide superconductors, first discovered in 1986 [49], remain superconducting at temperatures above the boiling point of liquid nitrogen. For example, two of the more common materials, $YBa_2Cu_3O_7$ and $Bi_2(Sr_2Ca)Cu_2O_8$, have $T_c \approx 93K$ and $T_c \approx 110$ K respectively. Technological interest in high T_c superconductors is based in part upon the fact that they require only liquid nitrogen, which is relatively cheap and readily available, as opposed to costlier liquid helium required to cool conventional superconductors. However, the practical utilisation of these materials has been difficult, owing to the fact that the oxide materials are hard to fabricate into useful form (e.g. wires).

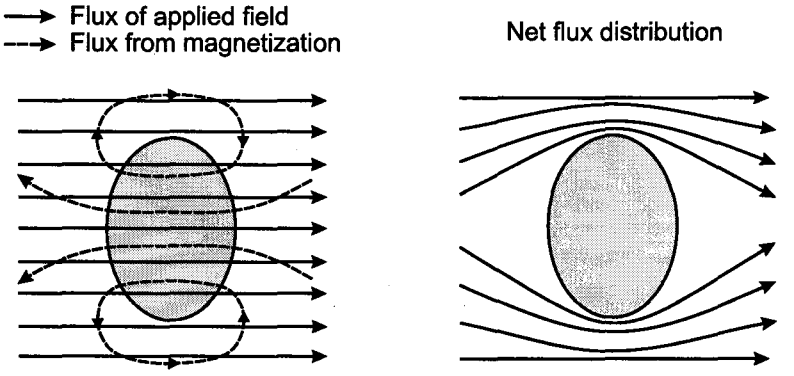

Figure 3.1: The superconductor exhibits perfect diamagnetism in magnetic fields smaller than H_c.

3.3 Perfect Diamagnetism and the Critical Field

The superconducting state can be destroyed not only by an increase in temperature above T_c, but also by the application of a sufficiently strong magnetic field, greater than the critical field, H_c. Ordinarily for fields less than H_c, the superconductor exhibits perfect diamagnetism, a phenomenon known as the Meissner-Ochsenfeld effect [50]. This is achieved via persistent screening currents which circulate on the surface, so as to cancel the flux density within (see Fig. 3.1), and occurs irrespective of the sequence with which temperature and field conditions are applied. This removal of the dependence of the state of the material upon the thermodynamic path distinguishes the superconductor from an ideal conductor.

For applied fields $H_a < H_c$, the Meissner effect ($\mathbf{B} = 0$) ensures that the magnetization $\mathbf{M} = -\mathbf{H_a}/4\pi$; in the normal state $\mathbf{M}$ is essentially zero. The work done on the sample by the magnetic field H_a is given by

$$-\int_0^{H_a} \mathbf{M} d\mathbf{H} = {H_a}^2/8\pi \tag{3.1}$$

and is stored in the free energy of the superconductor. The Helmholtz free energy density of a superconductor in a finite magnetic field H_a is given by

$$f_{sH} = f_{s0} + {H_a}^2/8\pi \tag{3.2}$$

where the free energy density of the superconductor in zero magnetic field is denoted

by f_{s0}.

At the critical field, the energy density difference between the normal (f_n) and superconducting (f_{sH}) state is zero, giving

$$\frac{H_c^2(T)}{8\pi} = f_n - f_{s0}. \tag{3.3}$$

3.4 The London Equations

The London theory, developed in 1935 and named for the brothers Fritz and Heinz London [51], was an early attempt to describe the magnetic behaviour of superconductors. While it did not address the specific microscopic mechanism underlying superconductivity, it did provide a phenomenological framework which successfully described both the absolute diamagnetism and the zero resistance to a dc current exhibited by superconductors. The theory is built upon the "two fluid model" [52], which postulates that the electrons in a superconductor may be considered as a mixture of two kinds of electrons, superconducting (of density n_s) and normal (of density n_n), with the total density of free electrons given by $n = n_s + n_n$. The resistanceless supercurrent is carried exclusively by the superconducting electrons, the density of which decreases from n to 0 as the temperature increases from 0 to T_c.

The London theory introduces two equations, in addition to Maxwell's equations, which govern the electromagnetic field within a superconductor. The theory begins with the equation of motion for superconducting electrons in an electric field $\mathbf{E}$

$$n_s m \frac{d\mathbf{v_s}}{dt} = n_s e\mathbf{E} \tag{3.4}$$

where m is the mass of the electron, e the electron charge, n_s the superconducting electron density, and $\mathbf{v_s}$ the velocity of the superconducting electrons. Given that $\mathbf{j_s} = n_s e\mathbf{v_s}$, this gives the first London equation

$$\frac{d\mathbf{j_s}}{dt} = \frac{n_s e^2}{m}\mathbf{E} \tag{3.5}$$

which describes the resistanceless property of a superconductor, since any electric field accelerates the superconducting electrons rather than simply sustaining their velocity against resistance, as described in Ohm's law in a normal conductor.[1] If we take the curl of both sides of Eq. 3.5 and use Maxwell's equation

$$\nabla \times \mathbf{E} = -\frac{1}{c}\frac{d\mathbf{B}}{dt} \tag{3.6}$$

this gives

$$\frac{d\mathbf{B}}{dt} = -\frac{mc}{n_s e^2}(\nabla \times \frac{d\mathbf{j_s}}{dt}). \tag{3.7}$$

Based on the experimentally observed Meissner effect, the flux density inside the superconductor is always zero (i.e. not just $d\mathbf{B}/dt$ but also $\mathbf{B}$ is zero within the bulk). To obtain this effect, the London brothers postulated that the superconductor might correctly be described by Eq. 3.7 applied to $\mathbf{B}$ instead of $d\mathbf{B}/dt$, that is

$$\mathbf{B} = -\frac{mc}{n_s e^2}\nabla \times \mathbf{j_s} \tag{3.8}$$

which is the second London equation, and describes the diamagnetism exhibited by the superconductor.

Using Maxwell's equation

$$\nabla \times \mathbf{B} = \frac{4\pi}{c}\mathbf{j_s} \tag{3.9}$$

and the relation

$$\nabla \times (\nabla \times \mathbf{A}) = \nabla(\nabla \cdot \mathbf{A}) - \nabla^2 \mathbf{A} \tag{3.10}$$

with Eq. 3.8 gives

$$\nabla^2 \mathbf{B} = \frac{1}{{\lambda_L}^2}\mathbf{B} \tag{3.11}$$

where

$$\lambda_L = \sqrt{\frac{mc^2}{4\pi n_s e^2}} \tag{3.12}$$

[1] In a normal metal, there is competition between scattering from defects and the acceleration by the electric field, leading to a steady-state drift velocity.

Element	Al	Hg	In	Nb	Pb	Sn	$YBa_2Cu_3O_7$
$\lambda_L(T=0)$ (nm)	50	38–45	64	35	39	51	150 (λ_{ab})

Table 3.2: London penetration depth at $T = 0$ for selected superconductors (from [53–55]).

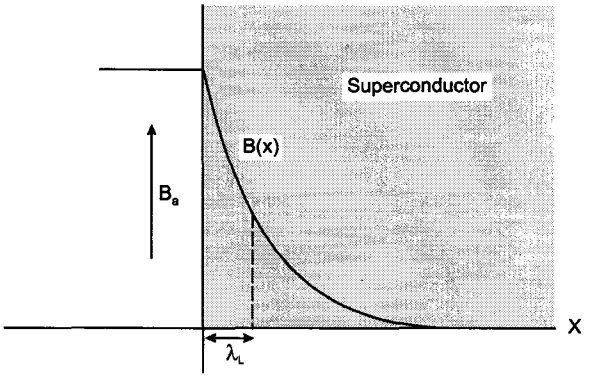

Figure 3.2: Penetration of magnetic flux into the surface of a superconductor (from [44]).

is the London penetration depth. It is within a surface layer of thickness λ_L that screening of the magnetic field takes place. The dependency on n_s gives λ_L a temperature dependence, which can be approximated by the empirical formula

$$\lambda_L(T) = \frac{\lambda(0)}{\sqrt{1-(T/T_c)^4}} \tag{3.13}$$

with values of $\lambda(0)$ for some conventional superconductors given in Table 3.2. Note that $\lambda_L \to \infty$ as $T \to T_c$.

For the case of a magnetic field applied parallel to a superconducting surface B_a, the London equations predict an exponential decay of the flux density within the superconductor, with characteristic decay length λ_L (see Fig. 3.2). The corresponding one-dimensional form of Eq. 3.11 gives

$$B(x) = B_a e^{-x/\lambda_L}. \tag{3.14}$$

In superconductors where the electronic mean free path l is limited by the presence of impurities, electrodynamic responses become more local. This results in an effective penetration depth $\lambda_{\text{eff}} > \lambda_L$. In this "dirty limit" ($l \ll \xi_0$), the relation is given by [56]

$$\lambda = \lambda_L \, (\xi_0/l)^{1/2} \qquad (\lambda \gg l, \xi_0 \gg l) \tag{3.15}$$

where the coherence length ξ_0 is the characteristic length scale over which the superconducting electron density varies (see Section 3.5). Most classical superconductors fall into the dirty limit, whereas the high T_c cuprate superconductors often approach the so-called "superclean" limit [57].

3.5 The Ginzburg-Landau Theory

While the London theory provided a fairly good description of the Meissner effect, there were several limitations. One shortcoming was the prediction of a negative surface energy for the interface between adjacent normal and superconducting regions. A superconductor in an external magnetic field would then prefer to exist as a series of alternating normal and superconducting regions, the size of which would be as small as possible so as to maximize the surface area. Experimental evidence however did not support these conclusions.

In 1950, Ginzburg and Landau formulated a theory [58] based on second-order phase transitions (the Landau theory), which gives a good macroscopic description of the superconducting state.[1] While still phenomenological, the Ginzburg-Landau (GL) theory uses quantum mechanics, in contrast to the London theory which is purely classical. It assumed that an effective wavefunction ψ described the behaviour of the superconducting electrons ($|\psi|^2$ is equal to the density of superconducting electrons), and was treated as a complex order parameter.

The theory also introduced two parameters: the first ξ, the Ginzburg-Landau coherence length, is the characteristic scale over which variations of the order parameter ψ occur ($|\psi|^2$ being 0 in a normal region, and 1 in a superconducting region). The second quantity λ, is the penetration depth for a weak magnetic field, indicating the

[1] As the GL theory is based on the Landau theory, it is valid only near the normal-superconducting phase boundary ($T_c - T \ll T_c$), and therefore not generally applicable at all temperatures.

characteristic length over which a magnetic field varies within a superconductor.

The GL theory was able to produce a positive surface energy term by incorporating quantum effects; the term arises from a gradient of the wavefunction at the normal-superconducting interface. In doing so, the GL theory in fact predicts the existence of two different classes of superconductors, now known as type I and type II.

3.6 Type I and Type II Superconductors

It had been thought for many years that all superconductors behaved as those described earlier, exhibiting the Meissner effect in an external magnetic field until superconductivity was destroyed at H_c. However, in 1957 Abrikosov postulated the existence of a different class of superconductor [59], now called type II, whose behaviour in an applied magnetic field differed from conventional expectations.

For type I superconductors, the normal-superconducting interface contributes a positive energy term. Hence the appearance of normal regions is energetically unfavourable, and the superconductor remains superconducting throughout when a magnetic field of strength less than H_c is applied. Type II superconductors however have a negative surface energy term, and as such it is favourable under certain conditions for the superconductor to split into an assemblage of superconducting and normal regions, entering the so-called "mixed state".

Type-I superconductors include all superconducting elements except niobium, while type-II superconductors include niobium as well as superconducting alloys and chemical compounds, including high T_c superconductors. The value of the ratio $\kappa = \lambda/\xi$, known as the Ginzburg-Landau parameter, distinguishes between type I superconductors ($\kappa < 1/\sqrt{2}$) and type II superconductors ($\kappa > 1/\sqrt{2}$).

3.7 The Mixed State

The negative energy of an interface between normal and superconducting regions in a type II superconductor implies that, under certain conditions of applied magnetic

field, it is energetically favourable for the superconductor to subdivide into normal and superconducting regions.

Consequently, a type II superconductor has both a lower and an upper critical field, denoted H_{c1} and H_{c2} respectively. For fields less than H_{c1}, type II superconductors behave in a similar manner to type I superconductors, exhibiting the Meissner effect. However, when the lower critical field is reached, it becomes more energetically favourable to let magnetic flux penetrate into the superconductor. This occurs for fields up to H_{c2} (which in fact is equal to $\sqrt{2}\kappa H_c$, and can be much greater than H_c), at which time the transition to the normal state occurs. A type II superconductor can therefore occupy two distinct superconducting states; the Meissner state, in which no flux is present in the interior of the material, and the mixed state, where the magnetic field partially penetrates the superconductor.

When the magnetic field penetrates a type II superconductor in the mixed state, it does so not in the form of laminar domains, but rather in the form of quantized vortex filaments. Each vortex is comprised of a normal (i.e. $n_s \rightarrow 0$) core, of radius $\sim \xi$, which can be approximated by a long thin cylinder, its axis parallel to the external magnetic field (see Fig. 3.3).

Recall that the bulk of the superconductor is diamagnetic, the flux due to the applied magnetic field being opposed by superconducting screening currents circulating along the perimeter of the specimen. However, within each core is magnetic flux, the direction of which is the same as that of the applied field. The flux within each core is thus generated by supercurrents which circulate around the normal core within an area of radius $\sim \lambda$, such that the magnetic field they generate coincides with that of the external field. These supercurrents are not transport currents, but are similar to the surface currents that shield the bulk of a type I superconductor. In addition, the circulating supercurrents encircling each normal core interact with the magnetic field produced by supercurrents of other normal cores, leading to a repulsive interaction between vortices.

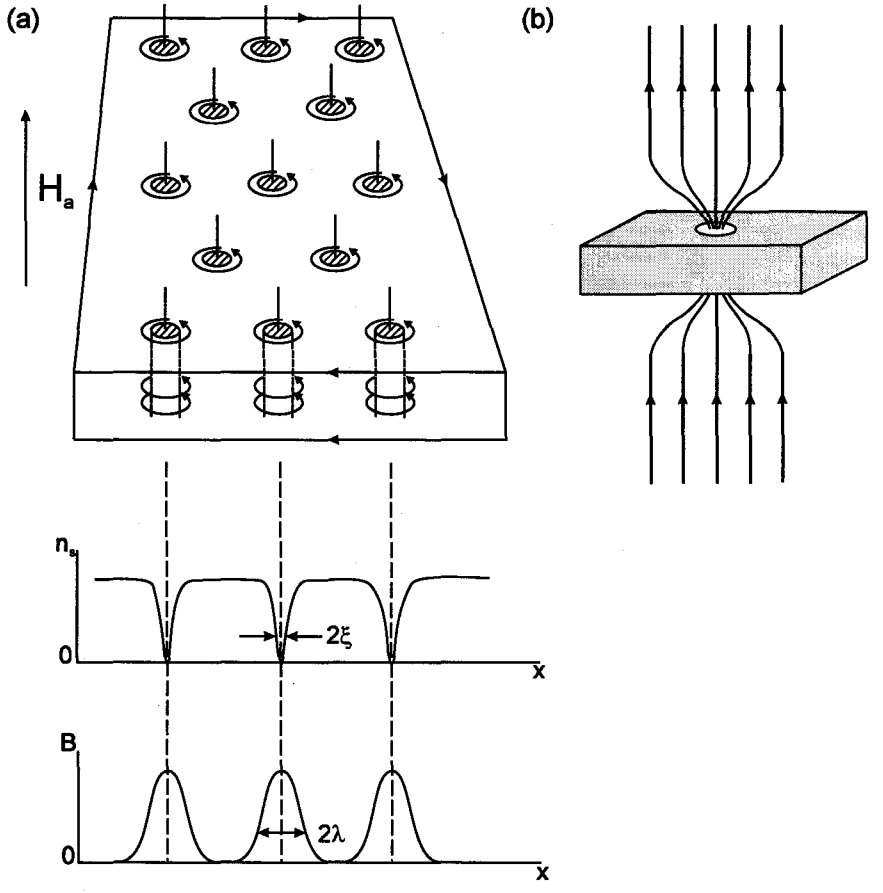

Figure 3.3: (a) Mixed state in an applied magnetic field H_a greater than H_{c1}, illustrating the normal cores and encircling supercurrents, as well as the characteristic lengths ξ and λ. (b) Magnetic field lines of a vortex as they pass through a thin superconducting sample.

The amount of flux carried by each vortex is quantized, and is given by

$$\Phi_0 = hc/2e \quad \text{(Gaussian units)} \tag{3.16}$$

$$= 2.07 \times 10^{-7}\ \mathrm{G\,cm^2} \tag{3.17}$$

$$= 2.07 \times 10^{-15}\ \mathrm{T\,m^2}, \tag{3.18}$$

a result that follows from the phase coherence of the electron wavefunction. Here h is Planck's constant and e is the electronic charge. Hence, any magnetic field penetrating a superconductor will be quantized, existing only as an integral multiple of the flux quantum Φ_0.[1] The values of the critical fields H_{c1} and H_{c2} can be defined in terms of the flux quantum, according to

$$H_{c1} = \frac{\Phi_0}{4\pi\lambda^2} \ln\left(\frac{\lambda}{\xi}\right) \tag{3.19}$$

and

$$H_{c2} = \frac{\Phi_0}{2\pi\xi^2}. \tag{3.20}$$

The penetration of these vortices occur once the applied field is increased beyond H_{c1}, at which point the vortices arrange themselves in a regular triangular array.[2] The nearest neighbor distance $a_\triangle$ between vortices in such an array is given by

$$a_\triangle = 1.075 \left(\frac{\Phi_0}{B}\right)^{1/2}. \tag{3.21}$$

As the field strength is increased, the vortex lattice period decreases and the density of vortices rises. At an applied field equal to H_{c2}, the distance between neighbouring

[1] Note that in cases where vortices are in close proximity to an edge, the amount of flux carried may be a non-integral value of the flux quantum [60]. While for bulk superconductors this effect diminishes quickly from the edge, the effect can persist farther into the material for the case of thin films [61,62]. Recent experimental work has confirmed this phenomenon [63].

[2] Though the triangular lattice is energetically the most favourable, in some monocrystalline type II materials (Nb, V, Tc, and Pb alloys) the underlying crystal structures dominate over the small theoretical energy differences, leading to square or even rectangular arrays of vortices.

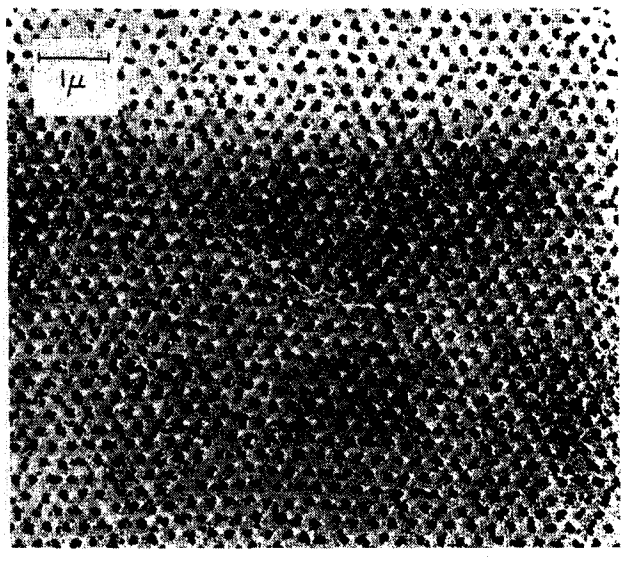

Figure 3.4: The triangular vortex lattice of a type II superconductor, as viewed using a magnetic decoration technique. From [64].

vortices is on the order of ξ, meaning that the normal cores of the vortices are in contact with each other and the sample is no longer superconducting.

The existence of the triangular vortex lattice was first experimentally verified in 1967 using a magnetic decoration technique [64]. As illustrated in Fig. 3.4, the electron microscopy picture shows a triangular pattern where small ($\sim$ 500 Å) ferromagnetic particles have settled on the surface of a magnetized lead–indium alloy at locations where the magnetic flux intersects the samples surface.

3.7.1 *Flux Flow*

In the presence of a transport current $\mathbf{J}$, vortices experience a Lorentz force $\mathbf{F} = \mathbf{J} \times \Phi_0/c$ per unit length, which tends to move the vortex transverse to the current. As they move with velocity $\mathbf{v}$, they induce an electric field of magnitude $\mathbf{E} = \mathbf{B} \times \mathbf{v}/c$, parallel to $\mathbf{J}$. The resulting energy dissipation $(\mathbf{E} \cdot \mathbf{J})$ across the bulk of the superconductor can lead to heating and a rise in temperature above T_c.

If the superconductor were free of defects, the vortices would begin moving with

the application of an infinitely small Lorentz force. The ability to sustain a persistent transport current therefore requires that vortex motion be restricted. Fortunately, the presence of an inhomogeneity can lead to vortices becoming pinned to fixed locations in the material, thereby preventing them from moving freely. Almost any kind of imperfection, the dimensions of which are as large or larger than the coherence length, can pin vortices. Examples include grain boundaries, atomic defects, or inclusions of non-superconducting material. As a result, there is essentially no resistance until a finite current is reached, at which point the Lorentz force exceeds the pinning strength and tears the vortices off the pinning centers. If the pinning is sufficiently strong, vortex motion can be made small enough so that the superconductor acts very much like a perfect conductor.

Typically one observes that for small values of applied current, such that the resulting Lorentz force is smaller then the pinning strength, no voltage (i.e. dissipation) is evident. As the current is increased, a finite nonlinear voltage appears at a certain value of current (the critical current). This corresponds to "flux creep", whereby the vortices jump randomly from one pinning site to another. As the current is further increased, the current-voltage characteristic becomes linear as the entire vortex structure as a whole undergoes motion, a process known as "flux flow".

It is clear that vortex pinning plays a very important role in determining the (critical) current carrying capability in type II superconductors. In fact, for type II superconductors in the mixed state, the critical current is almost completely controlled by the perfection of the material; the more imperfect the material the greater its critical current. From a technological point of view, there is great interest in understanding and controlling vortex pinning and motion. Some of the work presented in Chapter 4 is motivated by this goal.

4

Experimental Results and Discussion

The results presented in this chapter incorporate two experimental techniques. The first is magnetic force spectroscopy, whereby the resonance frequency of the cantilever is recorded as it is approached towards the sample at a single location. While not commonly employed, it is shown here to be a useful tool offering clear and easily interpretable results. The second, magnetic force microscopy imaging, involves scanning the cantilever with respect to the sample while recording a change in the cantilever status as a function of position. Together these complimentary techniques help to provide a more complete understanding of the properties of the sample.

Imaging of vortices was conducted under various conditions of scan height, temperature and applied magnetic field, and provide data which one can relate to such characteristics as the magnetic penetration depth and vortex pinning potentials. Magnetic force spectroscopy curves were acquired as a function of temperature in the absence of magnetic fields, and were used in the determination of the critical temperature T_c. All experiments were conducted on Nb thin film samples, the details of which are discussed below.

4.1 Sample Characteristics

Two samples were studied, both 100 nm thick Nb films deposited by magnetron sputtering onto silicon substrates.[1] One sample has a uniform coating of Nb, while

[1] The samples were kindly provided by V. Metlushko of the University of Illinois at Chicago, and B. Ilic of Cornell University.

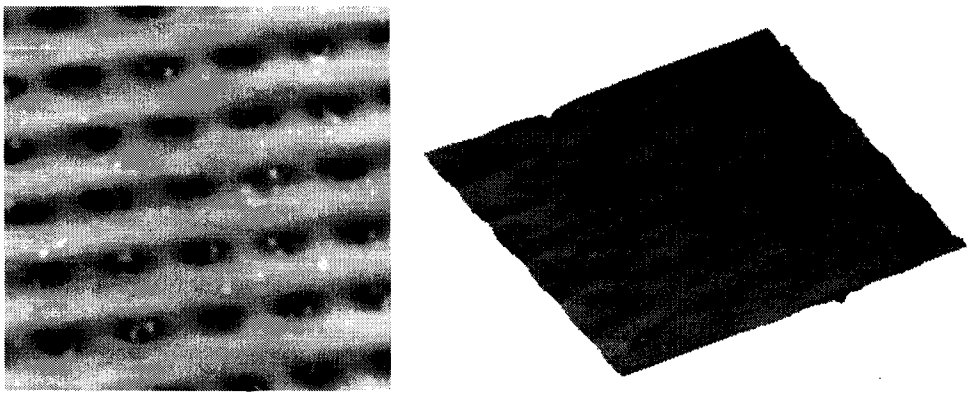

Figure 4.1: (Left)A 5×5 μm^2 area AFM image of the patterned Nb film, depicting the square lattice of antidots. The spacing between adjacent antidots is approximately 1 μm. (Right) A 3-D perspective view of the same image.

the other has been patterned with a square lattice of antidots (holes), of period 1 μm and diameter 0.3 μm, using laser interferometric lithography [65] (see Fig. 4.1). The purpose of the antidots is to serve as artificial pinning centers for magnetic vortices.

4.1.1 Artificial Pinning Centers

Recall that the movement of vortices is detrimental to a superconductor because it leads to energy dissipation, heating and the potential destruction of the superconducting state. Consequently, the behavior of magnetic vortices has a significant impact on the current carrying ability of a superconductor, including the maximum electrical current the superconductor can support. Current research efforts are directed towards the understanding and control of vortex motion, in an effort to increase the current carrying capacity of superconducting materials.

One such strategy is to introduce a regular lattice of artificial pinning centers, to provide strong pinning interactions and prevent vortex motion. The interplay between artificial pinning centers and the vortex lattice has been the focus of numerous studies in which one often observes anomalies in the temperature and magnetic field dependencies of the magnetization, electrical resistance and critical current responses [66–73]. These effects occur at "matching fields", so named because at these

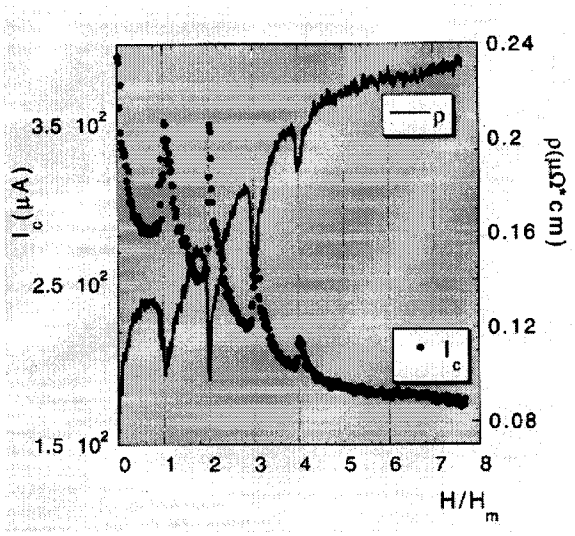

Figure 4.2: Critical current and resistivity measurements of the patterned Nb sample as a function of magnetic field, at T = 6.65 K. Adapted from [69].

magnetic field values the vortex lattice spacing becomes commensurate with the lattice of antidots, trapping a majority of vortices within the antidots. This effect is shown in Fig. 4.2, where sharp peaks in the critical current and resistivity of the patterned Nb film are observed at applied fields equal to multiples of the matching field, $H_m = nH_1$, where $H_1 = \Phi_0/d^2 \approx 20.7$ G, and n is an integer.

However, the number of vortices contained in each antidot for a given temperature is limited, and is given by the vortex saturation number [74]

$$v_s = D/4\xi(T) \tag{4.1}$$

where $D \approx 0.3$ μm is the antidot diameter, $\xi(T) = \xi_0/(1 - T/T_c)^{1/2}$, and $\xi_0 \approx 16$ nm for this sample [69]. The saturation number as a function of temperature, calculated using Eq. 4.1, is plotted for the patterned Nb sample in Fig. 4.3, although in practice the sputtering and lift-off lithography used to produce the antidots will result in some fluctuations of the hole diameter, leading to small variations in v_s between antidots. Any additional vortices are believed to form an Abrikosov lattice within the interstices of the antidot array [75].

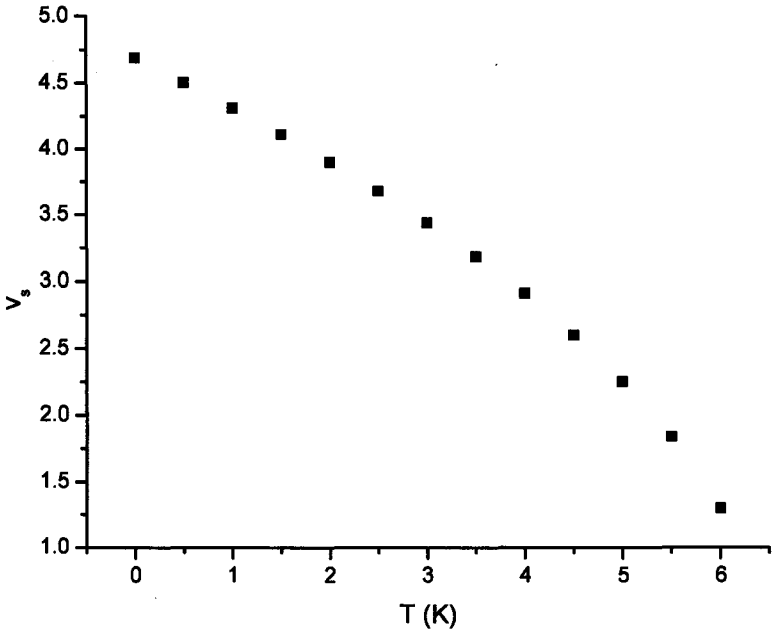

Figure 4.3: A plot of the calculated saturation number as a function of temperature for the patterned Nb film.

4.2 Experimental Details

Measurements of the unpatterned Nb film were made using two silicon nitride cantilevers, each made magnetically sensitive by the evaporation of 30 nm of Co onto one face of the pyramidal tip, which was magnetized along the tip axis prior to installation in the microscope. Both have nominal spring constants $k_{cb} = 0.1$ N/m, one with a resonance frequency $f = 32,398$ Hz and a quality factor $Q = 3,600$ (used for Fig. 4.5), the other with a resonance frequency $f = 36,585$ Hz and a quality factor $Q = 4,573$ (used for all other figures). The cantilever oscillation amplitudes ranged from $A = 20 - 30$ nm peak-to-peak.

Measurements of the patterned Nb film were also performed using two different silicon nitride cantilevers. The first, with which Figs. 4.21, 4.22 and 4.23 were acquired, had a resonance frequency $f = 30,793$ Hz, a nominal spring constant $k_{cb} = 0.1$ N/m, and a quality factor $Q = 14,664$. The oscillation amplitude was $A = 98$ nm peak-to-peak. The cantilever was coated with 40 nm of Co, evaporated onto one face of

the pyramidal tip, and magnetized along the tip direction prior to installation. The second cantilever, used to acquire Fig. 4.24, had a resonance frequency $f = 31,222$ Hz, a nominal spring constant $k_{cb} = 0.1$ N/m, and a quality factor $Q = 19,514$. The oscillation amplitude was $A = 50$ nm peak-to-peak. The cantilever was coated with 20 nm of Co, evaporated onto one face of the pyramidal tip, and magnetized along the tip direction, prior to installation.

In order to cancel the component of the earth's magnetic field perpendicular to the sample surface, a nulling magnetic field was applied along the z-axis using the superconducting solenoid. Measurements requiring zero-field environments were performed within the presence of the nulling field, and the magnitude of any applied fields were adjusted to compensate for the background stray field.

4.3 Magnetic Force Spectroscopy

4.3.1 Determination of the Critical Temperature

While in the superconducting state, the Meissner effect leads to the expulsion of flux for sufficiently small magnetic fields. The magnetic tip is a source of such a field, and as such the cantilever experiences a repulsive interaction when approached towards the sample surface, leading to an increase in the resonance frequency of the cantilever. The strength of this interaction, reflected in the magnitude of the change in the resonance frequency, serves as a gauge by which the critical temperature T_c can be determined.

Spectroscopy data shown in Fig. 4.4 plots the change in the resonance frequency of the cantilever as a function of tip-sample separation at various temperatures for the unpatterned Nb film. Each curve is comprised of 512 points, with a settle time of 0.02 s per point.

Large increases in the resonance frequency, indicative of a strong repulsive interaction, are observed at colder temperatures. At temperatures above T_c however, the superconductor is in the normal state; the Meissner effect vanishes, and there is no

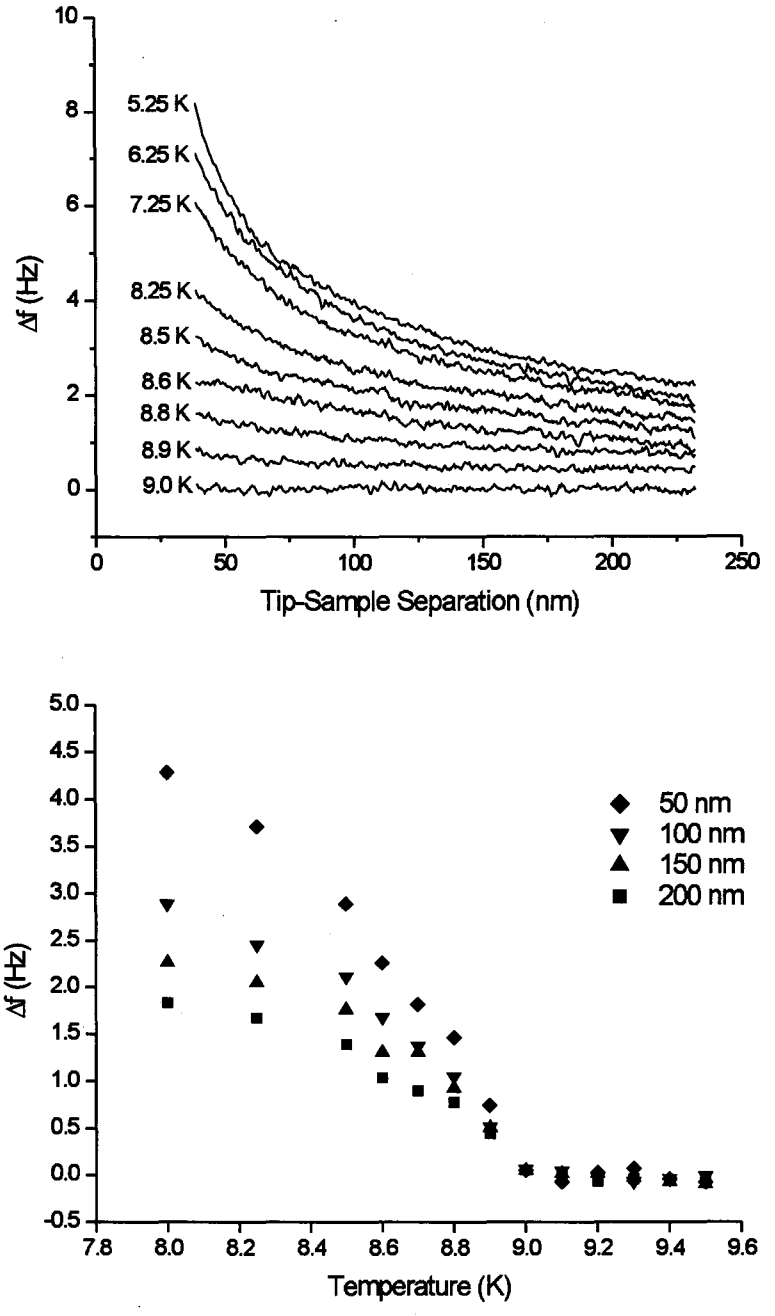

Figure 4.4: (Top) Resonance frequency shift versus tip-sample separation, at various temperatures for the unpatterned Nb film. Attractive interactions arising from van der Waals and electrostatic forces have been removed by subtracting the data from curves acquired at $T > T_c$. The strength of the repulsive interaction (Meissner effect) varies with the temperature. (Bottom) The same data, plotted as a function of temperature for various tip-sample separations. For temperatures $T \geq 9.0$ K, the magnetic interaction is negligible, suggesting that $T_c = 8.95 \pm 0.05$ K.

longer a magnetic interaction between the cantilever and the sample. This transition point is easily identified from a plot of the frequency shift of the cantilever versus temperature for various tip-sample separations, from which an estimate of T_c can directly be made. For the case of the unpatterned Nb film shown in Fig. 4.4, $T_c = 8.95 \pm 0.05$ K. The critical temperature for the patterned Nb sample was similarly determined to be $T_c = 6.50 \pm 0.05$ K.[1]

4.3.2 *Nucleation of Vortices by the Tip Magnetic Field*

Occasionally when the cantilever is approached towards the sample, the magnetic field from the tip will nucleate vortices [76]. This phenomenon is shown in Fig. 4.5, which illustrates two approach curves, both acquired at 7.9 K in a zero field environment, for the unpatterned Nb film. During vortex creation, the resonance frequency decreases discontinuously. This sharp reduction in the repulsive interaction occurs because the magnetic field of the vortex and the z-component of the tip magnetization are parallel, leading to a local attraction between the vortex and the magnetic tip.

Multiple vortices may be created, either simultaneously or in succession; the number of vortices created is reflected in the magnitude of the resonance frequency change. In Fig. 4.5 (a), two vortices are created simultaneously, producing a decrease in the resonance frequency of 0.4 Hz. Figure 4.5 (b) illustrates two vortices created in succession, with a 0.2 Hz shift observed for each vortex.

4.3.3 *Determination of the Magnetic Penetration Depth*

It was shown in Section 4.3.1 that as the magnetic tip is approached towards the superconducting sample, a repulsive interaction results. The variation in the strength of this interaction with temperature is a direct consequence of the temperature dependence of the magnetic penetration depth. At colder temperatures, any external magnetic flux is prevented from penetrating too deeply into the superconductor (i.e. λ

[1]The relatively low superconducting transition temperature, compared with the accepted value $T_c = 9.25$ K for bulk niobium, is due to a residual oxygen pressure in the growth chamber [69].

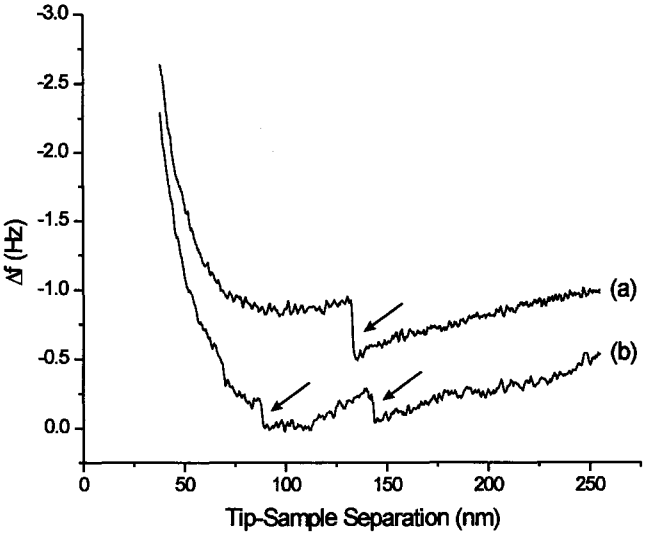

Figure 4.5: Resonance frequency shift versus tip-sample separation, at 7.9 K in zero applied field, for the unpatterned Nb film. The data includes attractive interactions resulting from van der Waals and electrostatic forces. Sharp discontinuities in the curve profiles (arrows) indicate the creation of vortices by the magnetic field of the tip. (a) Two vortices are created simultaneously, resulting in a change in the resonance frequency of 0.4 Hz. (b) Two vortices are created in succession, each contributing a 0.2 Hz change in the resonance frequency. The vertical axis of both curves has been offset for clarity.

is small); the associated screening currents result in a large repulsive Meissner force. As temperatures increase, flux penetrates more deeply into the superconductor (λ increases), until at T_c the superconductor passes into the normal state, $\lambda \rightarrow \infty$ and the superconductor becomes transparent to external magnetic flux.

Theoretical treatments in the literature [77–81] suggest that it is possible to determine the magnetic penetration depth from magnetic force spectroscopy data, such as that shown in Fig. 4.4 (Top). While numerous experimental methods are routinely employed to make bulk measurements of the penetration depth, including mutual inductance techniques [68], resonant LC circuits [82], microstrip resonators [83], muon spin rotation [84] and polarized neutron reflectometry [54], the growing interest in patterned and structured superconducting materials demands an ability to perform such characterizations on a local scale. Scanning probe techniques are therefore well suited to the task; both scanning SQUID [85] and scanning Hall probe [86,87] micro-

scopes have already been used to study high T_c materials in this regard.

A key advantage of MFM over these two scanning probe techniques however, is the ability to observe spatial variations in λ with a lateral resolution less than 100 nm, a feature afforded by the high spatial resolution achievable with MFM. As well, the MFM method requires relatively small sample sizes, typically several mm^2 down to a few 100 μm^2 in area. This feature is particularly desirable when dealing with exotic new materials, which are often difficult to grow to large sizes. In addition, the technique requires minimal sample preparation, and is relatively insensitive to surface conditions. Fast measurement times are on the order of minutes or less, and may commence immediately after the system has reached thermal equilibrium at the desired temperature.

It is with this aim that we have entered into a collaboration with Dr. A. Badía of the University of Zaragoza, Spain. Simulations based on code supplied by Dr. Badía and modified at McGill University were performed and compared with data acquired on the unpatterned Nb sample. The theory [81] models the vertical magnetic repulsive force between the superconductor and the extended magnetic tip a distance a above the surface as

$$F_z(a) = \frac{\mu_0}{4\pi}\int_0^\infty dk \int_V d^3\mathbf{r} \int_V d^3\mathbf{r}' \{k^3 C_{2xy}(k) e^{-2ak} e^{-k(z+z')} \times \left[\sum_{i,j} M_i(\mathbf{r}) g_{ij}(\mathbf{r}-\mathbf{r}') M_j(\mathbf{r}')\right]\}, \tag{4.2}$$

where $\mathbf{M(r)}$ is the tip magnetization function and V the volume of the tip. The volume integrations are performed with the origin of the coordinates at the lower end of the tip. The matrix elements g_{ij}, where the indices i, j indicate Cartesian components, are defined as

$$g_{ij} = \begin{cases} G_{ij} & i \neq 3 \\ -G_{ij} & i = 3 \end{cases}$$

and the matrix elements G_{ij} are defined as ($G_{ij} = G_{ji}$)

$$G_{11} = -\frac{1}{2}J_0(k\sqrt{x^2+y^2}) + \frac{x^2-y^2}{2(x^2+y^2)}J_2(k\sqrt{x^2+y^2})$$

$$G_{12} = \frac{xy}{x^2+y^2}J_2(k\sqrt{x^2+y^2})$$

$$G_{13} = -\frac{x}{\sqrt{x^2+y^2}}J_1(k\sqrt{x^2+y^2})$$

$$G_{22} = -\frac{1}{2}J_0(k\sqrt{x^2+y^2}) + \frac{y^2-x^2}{2(x^2+y^2)}J_2(k\sqrt{x^2+y^2})$$

$$G_{23} = -\frac{y}{\sqrt{x^2+y^2}}J_1(k\sqrt{x^2+y^2})$$

$$G_{33} = J_0(k\sqrt{x^2+y^2}) \tag{4.3}$$

The coupling coefficient C_{2xy}, which is a function of wavenumber k, the penetration depth λ, and film thickness b, contains all the information about the superconductor, and is defined as

$$C_{2xy}(k) = \frac{(\gamma^2-k^2)(1-e^{-2\gamma b})}{(\gamma+k)^2-(\gamma-k)^2e^{-2\gamma b}} \tag{4.4}$$

where $\gamma \equiv \sqrt{1/\lambda^2+k^2}$.

A comparison of the experimental and theoretical results are shown in Fig. 4.6. Here, the experimental data is the same as in Fig. 4.4, while the theoretical curves are plotted for selected values of λ appropriate for the temperature range.

It is clear that the simulated curves exhibit larger frequency shifts at smaller tip-sample separations, and a faster decay than the experimental data. They also appear to be converging to a singular value at some large tip-sample separation, whereas the experimental data does not demonstrate similar behavior.

The origin of the discrepancy between theoretical and experimental results lies with the tip magnetization model used for these calculations. For these simulations the volume V used for integration was taken to be the lower 200 nm portion (oxide sharpened region) of one face of the tip. We assume that the Co coating has the saturation magnetization of cobalt, that the film thickness is uniform, and that the domains are fully magnetized along the tip axis direction.

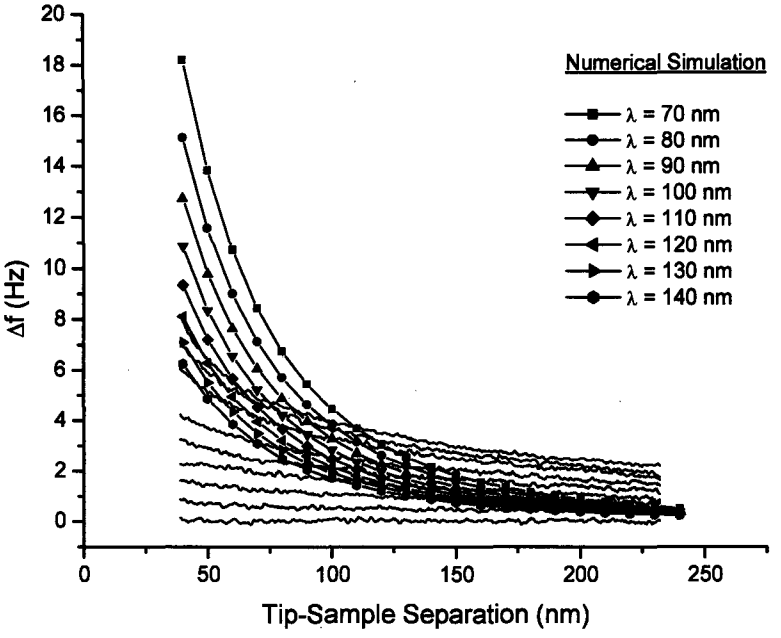

Figure 4.6: Experimental and simulated data of the resonance frequency shift versus tip-sample separation, for selected values of the magnetic penetration depth λ. The experimental data is the same as in Fig. 4.4.

In reality, after the tip is magnetized in an external field, the magnetic domain structure undergoes a relaxation, in order to minimize the magnetostatic energy. The magnitude of the resulting tip stray field is therefore less than the case of complete polarization. As well, the direction of the magnetization vector will not lie exactly along the tip axis, but will instead be subject to a re-orientation during the relaxation process.

These effects lead to a misrepresentation of the effective magnetic volume of the tip, resulting in a simulated response which does not reflect the experimentally observed results. Closer agreement between theoretical and experimental results necessitates a more realistic tip model. One possibility would be to incorporate a more complex tip structure derived from micromagnetic simulations, which calculate the domain structures of arbitrary geometries under a variety of initial conditions (see [88] for example). Alternatively, a quantitative analysis of the tip magnetization may prove useful, either using a simple tip model [89, 90] or through the use of a calibration

sample [91].

Even without a detailed knowledge of the micromagnetic tip structure, it may still be possible to extract from the data relative values of the penetration depth (i.e. λ_i/λ_1 $(i = 2,\ 3 \ldots\ N)$) in order to ascertain the temperature dependence of λ, a characteristic indicative of the underlying microscopic mechanism of superconductivity. This process is technically challenging however, requiring the use of numerical methods which perform inverse Laplace transforms of the experimental data. Work on this procedure is ongoing.

4.4 MFM Imaging of Vortices

One of the great strengths of magnetic force microscopy is its ability to produce real-space images of the magnetic structure of samples. Their pictorial nature often allows for a straightforward interpretation, offering a direct means by which to study the properties of magnetic vortices. In the following, MFM images of magnetic vortices are presented, acquired as a function of applied magnetic field, height and temperature.

4.4.1 Imaging as a Function of Applied Field

Vortices can be created by field cooling a superconductor in an external magnetic field. The number of vortices resident within a given area scales linearly with the applied field, according to

$$\text{Number of Vortices} = \frac{\text{Area}}{\Phi_0} \times \text{Magnetic Field}. \tag{4.5}$$

Figure 4.7 illustrates a sequence of MFM images acquired at selected field values, for the unpatterned Nb film. The superconducting solenoid was used to generate the magnetic field perpendicular to the sample surface. Strong pinning at randomly distributed material pinning sites prevents the formation of a regular Abrikosov lattice. The measured average inter-vortex separation as a function of field is shown in

Fig. 4.8, while the number of vortices in each image versus applied field is plotted in Fig. 4.9. The excellent agreement with the linear relation from Eq. 4.5 demonstrates that only single vortices, each carrying one flux quantum, are observed.

4.4.2 *Imaging as a Function of Height*

Constant height images employ no feedback, but instead record the *change* in the resonance frequency of the cantilever as the tip scans with respect to the sample. This mode of operation often demonstrates superior signal-to-noise and image quality over constant force gradient mode data.[1] Plane subtraction hardware is usually employed during the scanning process in order to ensure that the cantilever tracks parallel to the sample surface.

This mode of operation was used in order to acquire images as a function of height for the unpatterned Nb film. In preparation, the sample was heated to 10 K and a field of 5 G applied. This field strength was chosen in order to produce a sufficient number of vortices for study, but with enough inter-vortex spacing such that vortex-vortex interactions would be negligible. The sample was then cooled to 5 K, the applied field was removed, and a 5×5 μm^2 area was imaged at constant height as a function of tip-sample separation within a zero field environment. Scan heights were previously determined by approaching the tip to the sample surface at 10 K in zero applied field, until tip-sample contact was made.

Results are illustrated in Fig. 4.10, which show the change in the resonance frequency of the cantilever as a function of position. Cross sections through the middle vortex are also shown for each image. We see that the sharpness, as well as the amplitude of the peaks decrease with increasing scan height, a feature which follows from the expected decay of the magnetic field and field gradient with increasing tip-sample

[1] Constant force gradient operation typically requires the application of an electrostatic voltage for servoeing purposes. As a result, small magnetic signals are often masked by a dominant topographic signal. As well, any additional noise contributions associated with the feedback system are absent in constant height mode.

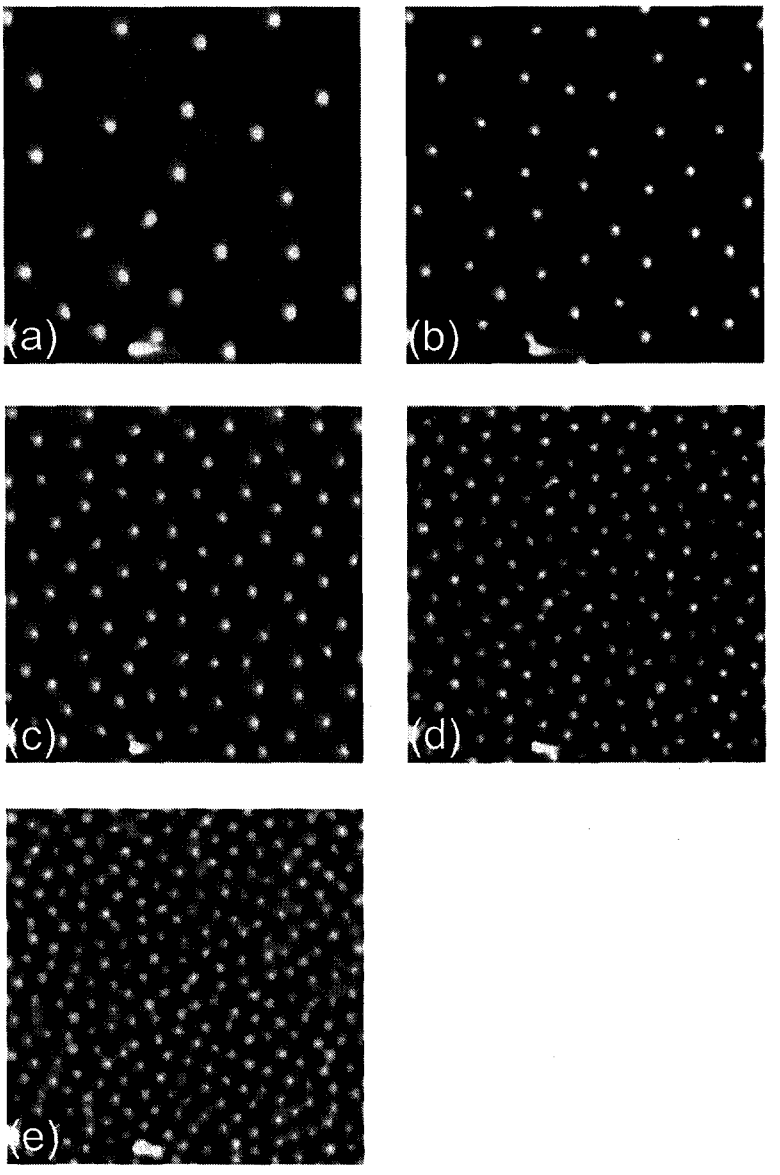

Figure 4.7: 10×10 μm^2 area MFM images of magnetic vortices for the unpatterned Nb film, all at 5 K. Fields correspond to (a) 5 G, (b) 10 G, (c) 20 G, (d) 40 G, and (e) 60 G. The images have been differentiated in the x-direction in order to enhance contrast. The structure at the bottom of each image is topographical in nature, and serves as a fiducial mark.

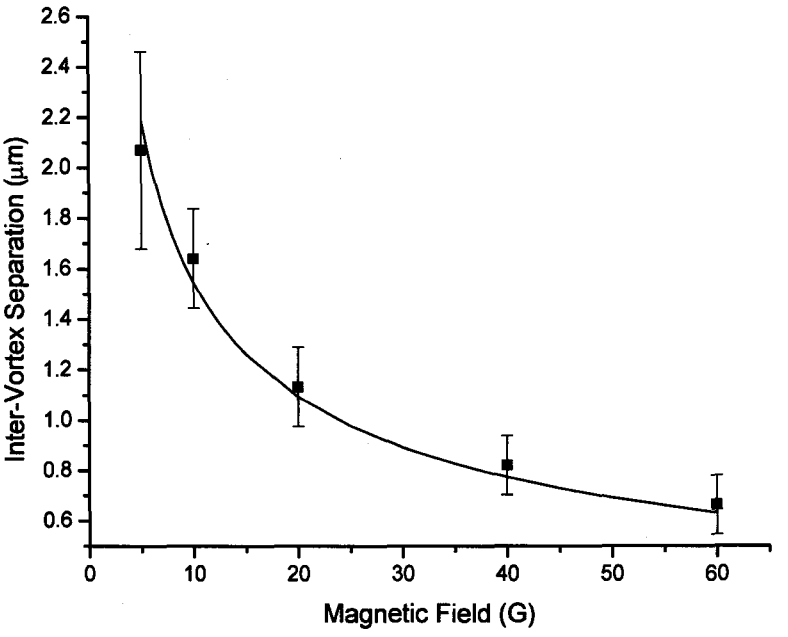

Figure 4.8: (symbols) The measured average inter-vortex separation as a function of applied magnetic field, for the vortices illustrated in Fig. 4.7. Error bars correspond to $\pm 1\sigma$. (line) The expected nearest neighbor distance for a triangular vortex lattice as given by Eq. 3.21.

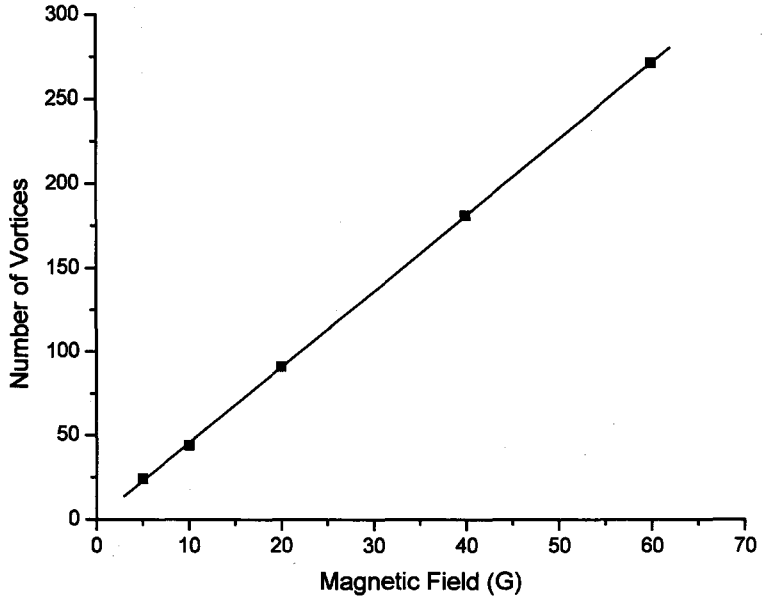

Figure 4.9: The number of vortices in Fig. 4.7, as a function of applied magnetic field. The expected linear relation is observed. A fit to the data yields a y-intercept of 0.4 ± 0.8 vortices, and a slope of 4.51 ± 0.02 vortices/G. This corresponds to a scan range of 9.7×9.7 μm^2, using the accepted value for Φ_0.

separation. The process was repeated for an applied magnetic field of equal magnitude and opposite polarity. The results are illustrated in Fig. 4.11, which employs the same scale as Fig. 4.10.

Light vortices correspond to a field parallel to the z-component of the tip magnetization, and produce an attractive interaction. Dark vortices correspond to a magnetic field anti-parallel to the z-component of the tip magnetization, and exhibit a repulsive interaction with the tip. While both figures share a common scale, the baseline offset has been independently adjusted in each case in order to maximize contrast; this accounts for the discrepancy in the background value between the two figures.

One immediate conclusion that can be drawn from the data in Figures 4.10 and 4.11 is that for Nb, the dominant interaction observed by MFM is that of the tip magnetic moment with the stray field of the vortex. An interaction dominated by the absence or weakening of the Meissner effect over the normal conducting core of a vortex would lead only to constant contrast irrespective of the vortex polarity, as opposed to the observed contrast reversal between attractive and repulsive vortices. As well, both attractive and repulsive vortices exhibit similar size, shape and interaction strengths (i.e. frequency shifts), and appear to differ only in polarity, as expected.

Given that magnetic force microscopy is sensitive to the magnetic stray field produced by the vortices, and that the size of the vortices is determined in part by the magnetic penetration depth λ of the material, one is naturally led to the question of whether it is possible to extract a value for λ based on the images in Figures 4.10 and 4.11.

A direct measure of the observed vortex radius will not yield the correct value for λ; in general the radius of a vortex is not equal to the penetration depth. However, numerical simulations [92–94] can model the vortex profile given a particular value for λ. Sample calculations based on code supplied by O. Fritz [92] are shown in Fig. 4.12, which illustrates the vortex profile at the surface of the superconductor, for two different values of $\kappa = \lambda/\xi$. Both the first and second derivatives of the

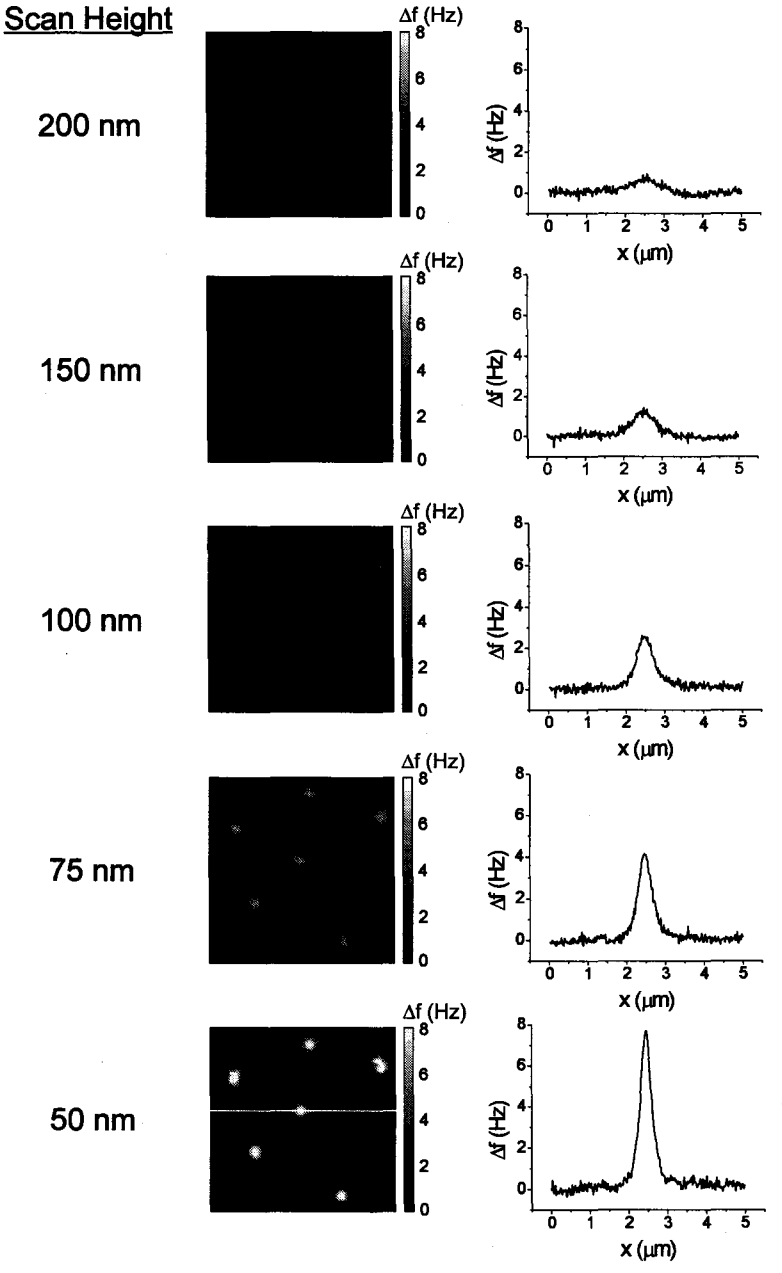

Figure 4.10: 5×5 μm^2 area MFM images for the unpatterned Nb film, acquired at 5K, at various scan heights. A field of 5 G was used to generate the vortices. The full scale of 0 to 8 Hz is identical for all images. Here attractive interactions correspond to an increase in Δf (i.e. lighter colours). Also shown are corresponding cross sections in the x-direction through the middle vortex, the location of which is indicated by the white line in the 50 nm image.

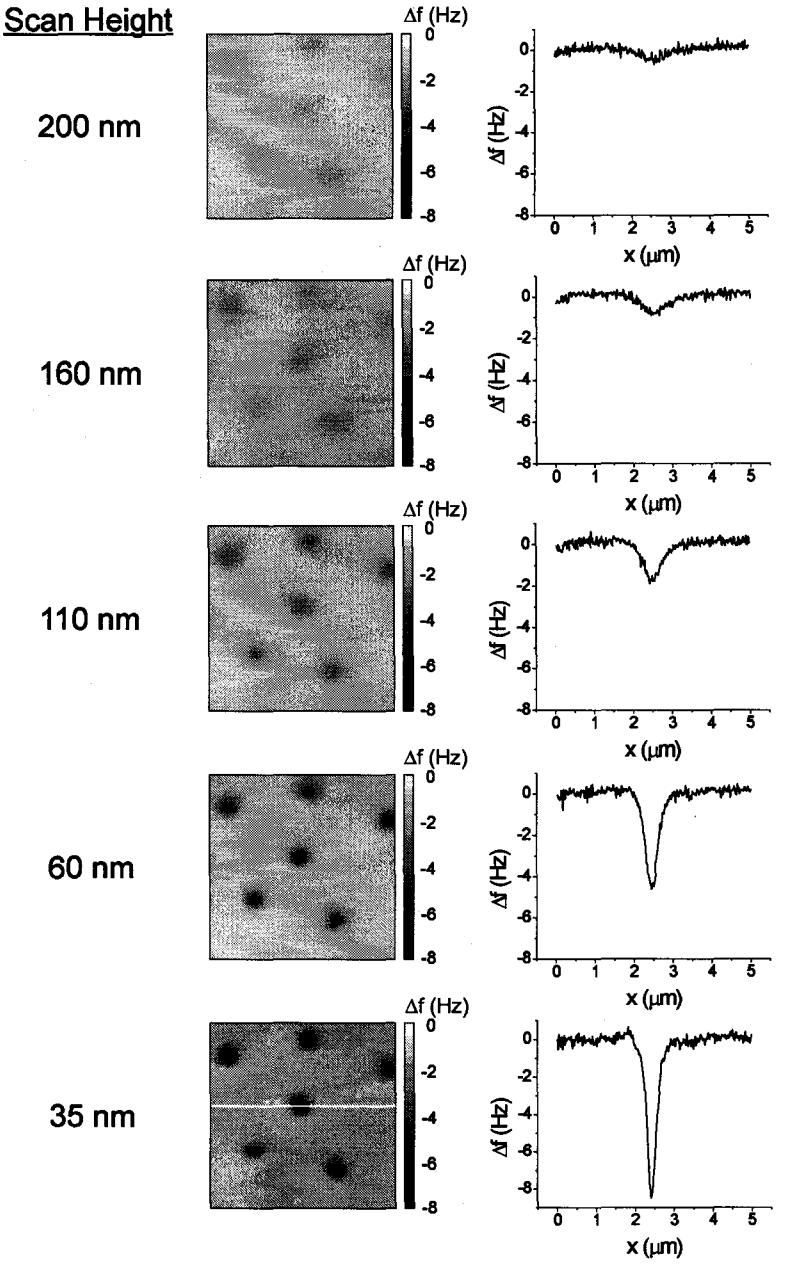

Figure 4.11: 5×5 μm^2 area MFM images for the unpatterned Nb film, acquired at 5K, at various scan heights. A field of -5 G was used to generate the vortices. The full scale of 0 to -8 Hz is identical for all images. Here repulsive interactions correspond to a decrease in Δf (i.e. darker colours). Also shown are corresponding cross sections in the x-direction through the middle vortex, the location of which is indicated by the white line in the 35 nm image.

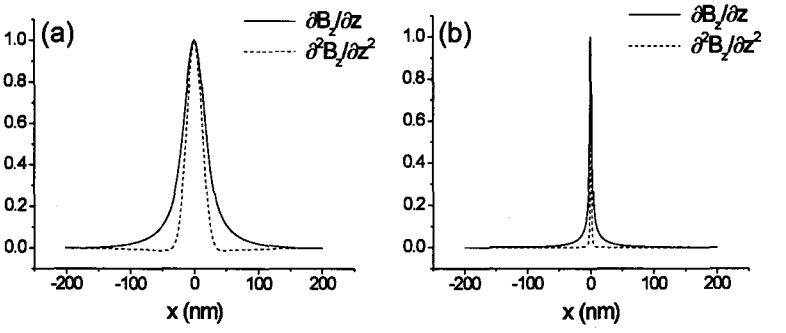

Figure 4.12: The normalized first and second derivatives of the z-component of the stray field of a vortex, calculated at the surface of the superconductor. (a) For Nb ($\kappa \sim 1$). (b) For a high κ material ($\kappa \sim 100$), such as the high T_c superconductor YBCO.

z-component of the stray field are plotted, the relevant form depending on whether the monopole or dipole tip model is used [3].

Note that in general it is more difficult to image low κ materials due to their wide vortex profiles; the more spatially diffuse the magnetic field, the smaller the field gradient and resulting tip-sample interaction. Conversely, high κ materials exhibit narrow vortex profiles, producing more localized field gradients which are more easily imaged by MFM.

The following analysis adopts the monopole tip model, a reasonable assumption based on the fact that the decay length of the vortex field (on the order of 200 nm - see Figures 4.10 and 4.11) is small compared with the dimensions of the magnetic volume of our tip (several μm). This approximation is also supported by the qualitative similarity between the $\partial B_z/\partial z$ curves of Fig. 4.12 and the cross sections in Figures 4.10 and 4.11, especially for tip-sample separations greater than 50 nm.

Figure 4.13 plots the experimentally determined half width at half maximum (HWHM) for all vortices in Figures 4.10 and 4.11, as a function of height. Also included are theoretical curves of the half width at half maximum for three values of λ; $\lambda = 45$ nm, $\lambda = 90$ nm, and $\lambda = 180$ nm. These values were chosen based on the estimation of $\lambda(\mathrm{T} = 5\ \mathrm{K}) = 90$ nm, calculated using the dirty limit expression (Eq. 3.15) where $\xi_0 \approx 27$ nm and $l \approx 4.5$ nm for this sample [95], and $\lambda_{\mathrm{L}}(\mathrm{T} = 0\ \mathrm{K}) = 35$ nm for

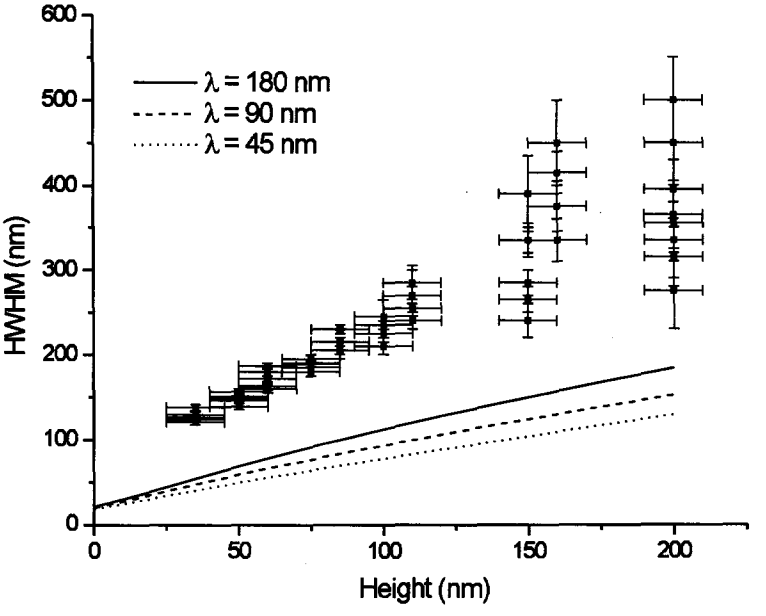

Figure 4.13: The half width at half maximum (HWHM) of all vortices in Figures 4.10 and 4.11, plotted as a function of scan height. The increase in uncertainties at larger scan heights results from a reduction in the signal-to-noise ratio. Also shown are theoretical curves for three different values of λ.

Nb [54]. There is good qualitative agreement between the experimental and theoretical plots. However, an obvious quantitative disagreement exists, with the theoretical estimates of the HWHM a factor of ~ 2.5 times smaller than observed experimentally.

This discrepancy arises from the fact that the observed vortex profile is a convolution between the vortex stray field and the extended tip geometry. In order to deconvolve the data and extract the pure vortex profile, a detailed knowledge of the magnetization structure of the tip is required. Such an analysis is highly non-trivial to perform, and has so far only been demonstrated on Cu/Ni/Cu samples [91]. If such a calibration procedure were to be extended and applied to this situation, it would then be possible to obtain a numerical estimate of λ. The accuracy with which λ can be measured can be estimated to first order by applying a linear fit to the experimental data in Fig. 4.13, yielding a slope of 1.6 ± 0.1. The error in the slope corresponds to an uncertainty in the value of λ of between 10–20% (e.g. the theoretical curve for

$\lambda = 180$ nm has a slope of 0.82(2); the simple ratio $180/0.82 = x/0.1$ yields an error for λ of $x = 22$ nm, or approximately 12%).

4.4.3 *Dissipation Images of Vortices*

Magnetic dissipation force microscopy offers a way to probe the non-conservative interactions between the tip and the sample, and often allows for the visualization of structures not easily seen in conventional MFM images [36,96,97]. In this technique, the damping of the oscillating tip is measured simultaneously with the usual frequency shifts associated with tip-sample force gradient variations. Dissipation images presented here were acquired in constant amplitude mode, using a separate feedback system to adjust the cantilever drive amplitude.

Constant height and corresponding dissipation images of vortices acquired for the unpatterned Nb film are illustrated in Fig. 4.14. The sample was field cooled from 10 K in a 5 G field in order to generate the vortices. At 5 K, the field was removed and imaging was performed in a zero field environment. Figures 4.14 (a) and (c) are similar to those in Figs. 4.10 and 4.11, which illustrate the resonance frequency shift of the cantilever. The dissipation images of Figs. 4.14 (b) and (d) are particularly interesting, owing to the fact that the location of the vortices is clearly indicated. Note also the contrast reversal between the two images; at a tip-sample separation of 40 nm, dissipation across a vortex is greater than that of the surrounding region, whereas at a scan height of 15 nm, dissipation associated with the vortex is less than that of the surrounding region.

Cross sections of the dissipation images for the two scan heights are shown in Fig. 4.15 (a). The difference in the baseline energy loss in one oscillation cycle of the cantilever is calculated to be 4.3×10^{-22} J, approximately 10 times larger than the energy associated with the thermal motion of the cantilever at 5 K. This baseline shift is believed to result from an increase in eddy current damping at reduced scan heights. Recall that supercurrents on the sample surface act to screen the magnetic stray field

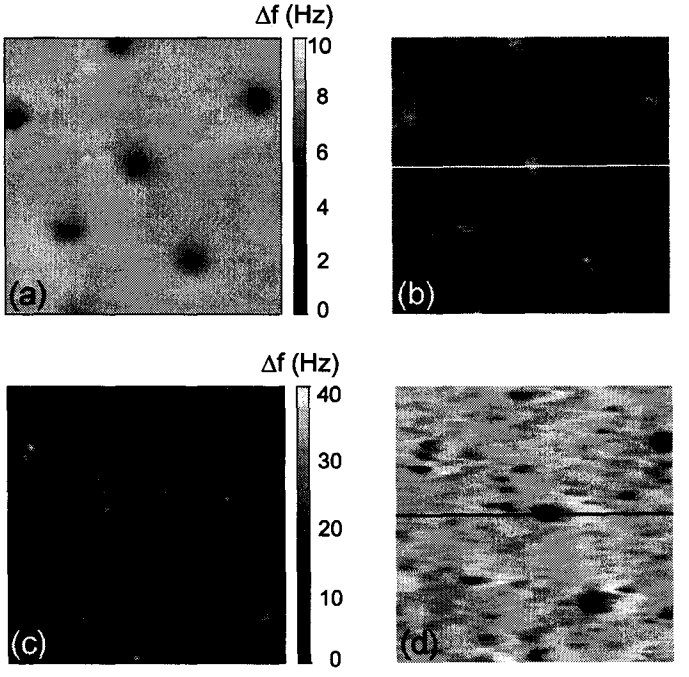

Figure 4.14: Resonance frequency shift and dissipation images for the unpatterned Nb film. (a) Resonance frequency shift and (b) corresponding dissipation signal at a constant scan height of 40 nm. (c) Resonance frequency shift and (d) corresponding dissipation signal at a constant scan height of 15 nm. Lines in (b) and (d) illustrate the position of cross sections shown in Fig. 4.15. The baseline offset in (a) and (c) has been independently adjusted in each case in order to maximize contrast. A field of 5 G was used to generate the vortices. All images are 5×5 μm^2 in area, acquired at 5 K.

of the tip. These supercurrents induce eddy currents in the tip, an effect that increases as tip-sample separations decrease. Note however that this effect occurs only over the superconducting regions of the sample, and not over the normal conducting cores of the vortices.

The dissipation signal across a vortex is interpreted as being an indication of tip induced motion of the vortex within its potential well, where the associated energy cost is related to the steepness of the walls of the well. As shown in Fig. 4.15 (b), at larger tip-sample separations (40 nm) the vortex pinning potential landscape is only weakly disturbed by the repulsive stray field of the tip, and the vortex is pinned within a deep potential well. At smaller tip-sample separations (15 nm) the energy

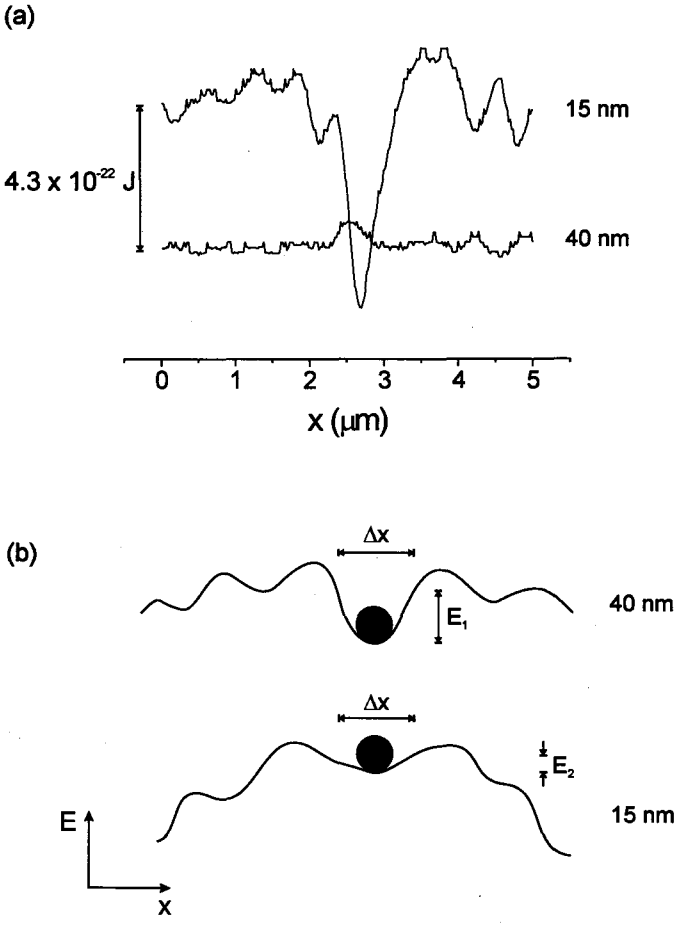

Figure 4.15: (a) Cross section of dissipation data from Figs. 4.14 (b) and (d). The difference in energy loss in one oscillation cycle is 4.3×10^{-22} J. (b) Schematic illustration of corresponding vortex pinning potential landscape. Black circles represent the vortices. For a given distance Δx by which interactions with the tip wiggle the vortex, the corresponding energy cost varies with the depth of the well (E_1 at 40 nm tip-sample separation, E_2 at 15 nm tip-sample separation).

landscape is more strongly distorted, and potential wells become flatter. For a given distance Δx by which tip interactions "wiggle" the vortices, the associated energy costs vary depending on the potential well profile, with more energy dissipated over vortices at larger tip-sample separations (E_1) than at smaller tip-sample separations (E_2).

4.4.4 *Imaging as a Function of Temperature*

As the temperature of a superconductor rises towards T_c, the mobility of vortices increases, facilitated by an increase in thermal energy. This increase allows vortices to hop from one pinning site to another in response to a driving force, typically arising from transport currents (Lorentz force) or the thermal force of a temperature gradient [57].[1] The Anderson-Kim theory [98] assumes a thermally activated hopping rate R of the form

$$R = \omega_0 \, e^{-F_0/kT} \tag{4.6}$$

where ω_0 is some characteristic frequency of vortex-line vibration, unknown in detail, but assumed to lie in the range from 10^5 to 10^{11} sec^{-1}, F_0 is the barrier energy, k is Boltzmann's constant, and T is the temperature. Unfortunately, lengths such as the distance between and the width of pinning centers enter the theory in ways which are imperfectly known, making exact calculations difficult [45]. Consequently, in the following we restrict ourselves to a semi-quantitative analysis.

Images as a function of temperature for the unpatterned Nb film are shown in Fig. 4.16, acquired with a constant tip-sample separation of 75 nm. Prior to imaging, the sample was field cooled within a 4.14 G field in order to generate $\sim$ 20 vortices within the 10×10 μm^2 scan area. A nulling field was subsequently applied to ensure image acquisition in a zero field environment.

At temperatures below 6.0 K pinning is sufficiently strong so as to prevent any

[1] Motion of vortices due solely to a thermally activated process is often negligible at temperatures associated with conventional superconductors.

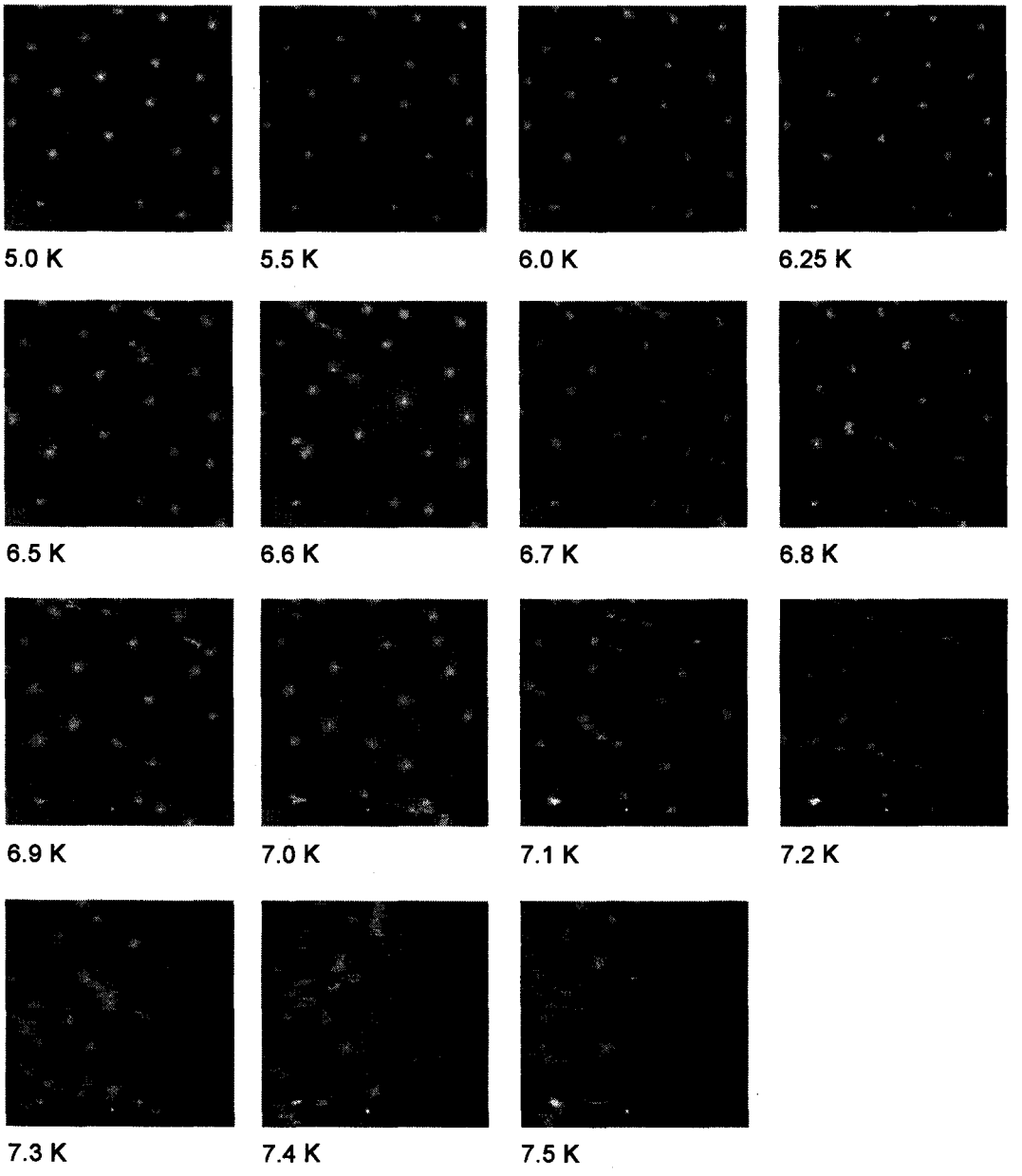

Figure 4.16: Temperature sequence of 10 × 10 μm^2 constant height images (75 nm tip-sample separation), illustrating vortex motion. As temperatures increase, the vortices are more weakly pinned and are more easily influenced by the magnetic field of the tip, which provides a driving force to the left.

tip induced motion of vortices. The first occurrence of vortex motion occurs at 6.0 K, with increasing numbers of vortices moving as temperatures rise. Often vortices become dislodged during scanning while the magnetic tip is directly above, appearing as streaks flowing towards the left side of the image, and producing an image of the vortex which is elongated and laterally displaced. At 7.2 K most vortices are no longer pinned, and by 7.5 K only a few vortices remain distinguishable.

The trajectories of the vortices as a function of temperature are shown in Fig. 4.17, superimposed on the 5.5 K image from Fig. 4.16. Note that on several occasions, vacated pinning sites become re-occupied by other vortices. The fact that vortices cannot be easily differentiated from one another as temperatures increase is a major impediment to any quantitative analysis. Most time-resolved studies are performed at constant temperature, employ transport currents or time varying magnetic fields in order to induce vortex motion, and have a sufficiently large field of view such that the trajectory of individual vortices can be more easily observed [99–101].

Figure 4.18 plots the distance traveled by each vortex ("hopping" distance) in Fig. 4.17 as a function of temperature. Two observations can immediately be made. Firstly, vortices appear to move larger distances at higher temperatures, and in fact the maximum distance seems to increase with temperature in an exponential-like fashion. Secondly, the spread of distances also appears to increase with temperature.

In the experiments presented here, the source of the driving force on the vortices is not a transport current, but rather the stray field of the tip; such an effect has not previously been demonstrated in the literature. The resulting force on the vortices to the left arises from the dipolar nature of the tip, which produces a magnetic field opposite in polarity to the vortices on the right side of the tip, and similar in polarity to the vortices on the left side of the tip. This is shown in Fig. 4.19, which illustrates the calculated tip stray field at the sample surface; note that Bz is negative in the region x>0. The origin of the driving force may then be understood as follows: as the tip scans from right to left, vortices are attracted to the tip while to its right, and

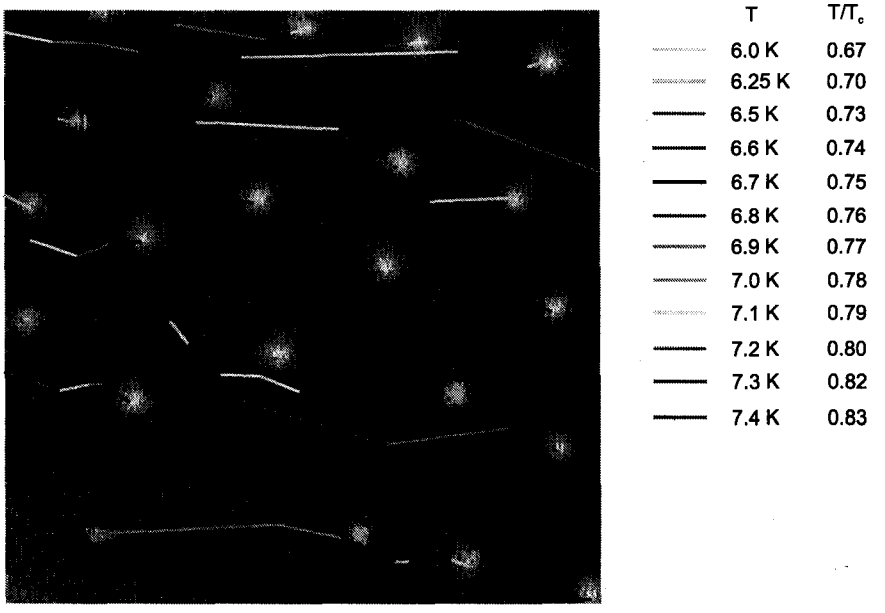

Figure 4.17: The trajectories of the vortices as a function of temperature, superimposed on the 5.5 K image from Fig. 4.16.

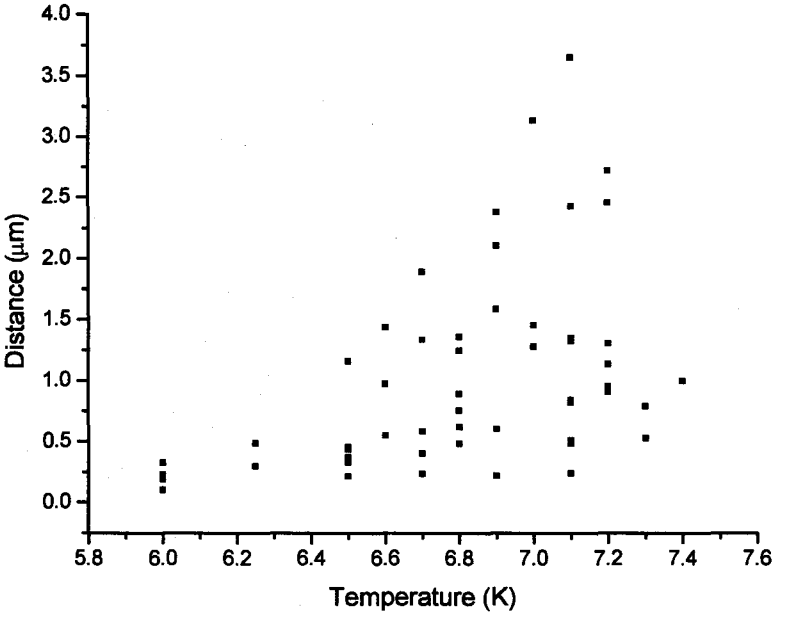

Figure 4.18: The distance traveled by each vortex in Fig. 4.17, as a function of temperature. Errors on distance measurements correspond to approximately 100 nm.

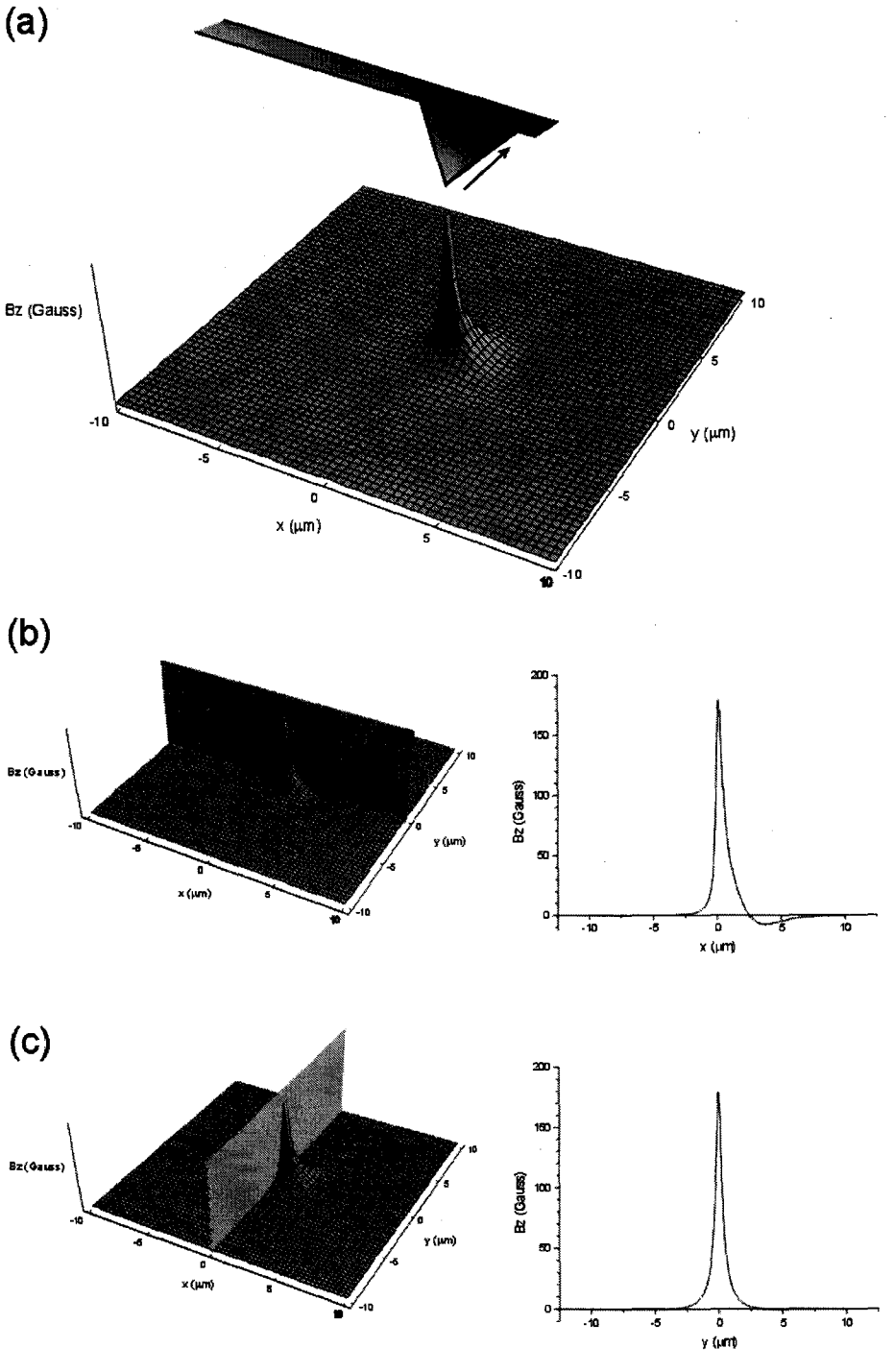

Figure 4.19: (a) Simulation of the magnetic field from the tip, located at a height of 200 nm above the superconductor, at the sample surface. The tip magnetization direction is indicated by the arrow. (b) and (c) depict cross sections through the x=0 and y=0 planes. Note the field of negative magnitude in (b), which produces vortices with a field anti-parallel to the z-component of the tip magnetization direction.

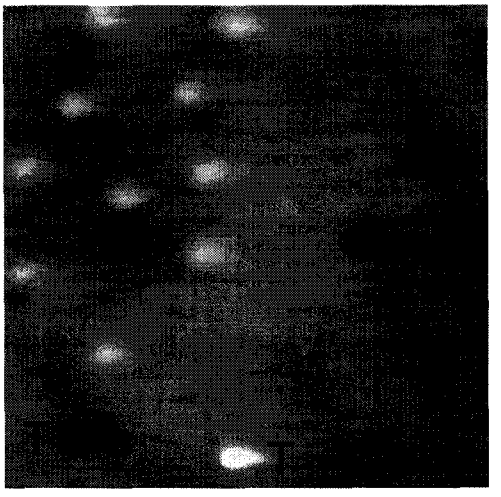

Figure 4.20: $10 \times 10\ \mu m^2$ area MFM image, acquired at 5 K within a nulling field, depicting vortices generated by the magnetic stray field of the tip. The tip was located approximately 200 nm above the sample surface. Vortices of both polarities are observed. The two bottommost structures, marked T, are topographical in nature.

are repelled from the tip while to its left. The net result is a force on each vortex to the left.

The dipolar nature of the tip stray field may be directly observed by imaging vortices induced by the tip, as shown in Fig. 4.20. Vortices were nucleated by thermally cycling the sample above T_c and back to 5 K with a nulling field applied, during which time the tip was located at the center of the scan region, approximately 200 nm above the surface. While this technique offers one the ability to directly visualize the tip stray field, a quantitative determination of the field strength based on vortex number, from which the tip magnetization might be reconstructed, is problematic.

There are two principal reasons for this. Firstly, an energy analysis to determine the conditions of vortex creation is non-trivial, often requiring mathematical simplifications such as the modeling of the tip as a point dipole, which limits its ability to faithfully reproduce the experimental data. Secondly, vortices which are created remain highly mobile as the sample is cooled through T_c. Depending on the strength of local pinning centers, which restrict vortex motion, attractive pairs of oppositely polarized vortices may annihilate each other before vortex motion is com-

pletely suppressed. This appears to be the case in Fig. 4.20, where it is estimated that approximately 3 vortex pairs were annihilated, leaving an empty region between the surviving attractive and repulsive vortices. Consequently, the vortices shown in Fig. 4.20 are representative of though not strictly equivalent to the tip stray field.

4.4.5 *Imaging the Patterned Nb Film*

Superconducting films patterned with arrays have been studied in the past in order to measure such effects as the influence of surface structures on the critical field and vortex configuration [73, 102, 103]. In these experiments vortices were visualized using the Bitter method. With this technique however, an additional superconducting layer is required underneath the array, in order to turn coreless vortices formed in the array into Abrikosov vortices which may then be decorated with magnetic particles. The tacit underlying assumption is that the presence of this underlayer does not significantly alter the physical properties under study. As well, the Bitter method cannot provide information on dynamic processes, and of course its "single shot" nature means that a sample can only be imaged once.

The increasing technological importance of patterned superconducting structures necessitates that further studies be undertaken by more novel and flexible techniques, which do not suffer the same limitations as the Bitter method. It is for this reason that the expertise demonstrated in the preceding sections have been applied towards the study of the patterned Nb film. The work was undertaken with the aim of achieving a better understanding of the interaction between vortices and artificial pinning centers. The intent was to acquire images as a function of applied magnetic field for $T/T_c > 0.955$ (such that $v_s = 1$), in order to compare vortex configurations with theoretical simulations [75]. However, repeated attempts to image vortices at temperatures $T/T_c > 0.955$ yielded no observable magnetic contrast. In retrospect this is not a surprising phenomenon. As shown in Fig. 4.16, magnetic contrast deteriorates as temperatures increase; a similar effect here would preclude imaging at elevated

temperatures.

Subsequent experiments at reduced temperatures succeeded in imaging magnetic vortices, as shown in Fig. 4.21. These images highlight the sensitivity of the magnetic contrast to temperature; the impact of variations as small as 0.1 K are clearly noticeable with regard to the magnetic contrast, while the topographic contrast (dark regions corresponding to the antidots) remains unchanged. Aside from the issue of contrast however, it is clear that these vortices show similar "cloud" like and streaky characteristics as those in Fig. 4.16. Clearly, at these temperatures the vortices are only weakly pinned, and are easily influenced by the magnetic field of the tip during image acquisition. This is consistent with results for the unpatterned sample, which exhibited significant vortex motion at $T/T_c \sim 80\%$; here, 5.7 K corresponds to $T/T_c \sim 88\%$ for the patterned film, and a similar effect is both anticipated and observed. The strong tip influence is further demonstrated in Fig. 4.22, which illustrates the effect of the scan direction on the observed vortex structure.

Note that the observed spatial offset between the center of the antidots and the vortices can be attributed to the fact that topographical and magnetic contrasts arise from two different regions of the tip. Whereas the tip apex is the relevant region for topographic features, magnetic images derive from the magnetic coating on one side of the tip. The displacement of these regions within the tip is reflected in the observed offset of the features in the images.

Images as a function of magnetic field are illustrated in Fig. 4.23. It was found that for applied fields less than 41.4 G (H_2), no magnetic structure was observed, while fields of 82.8 G (H_4) and greater produced images with a muddled appearance. The latter effect likely results from the progressive overlapping of adjacent vortices as field strengths increase, making the boundaries of individual vortices difficult to distinguish.

The fact that no structure is observed for field values smaller than H_2 is consistent with the fact that at these temperatures, each antidot is able to accommodate more

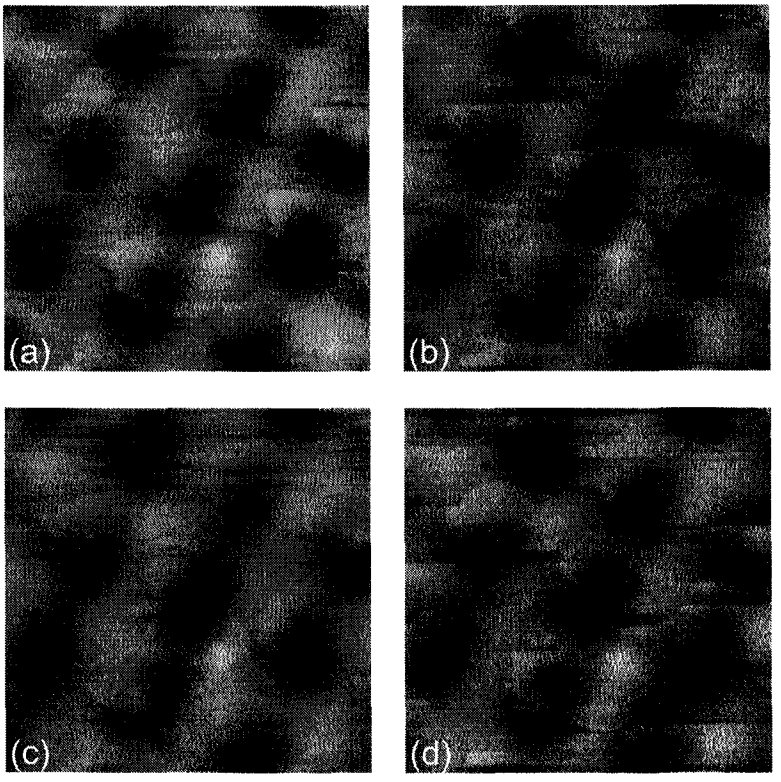

Figure 4.21: $2.5 \times 2.5\ \mu m^2$ area MFM images, acquired in 62.1 G (H_3), at (a) 5.7 K, (b) 5.8 K, (c) 5.9 K, and (d) 5.7 K again. Magnetic contrast diminishes with increasing temperature, while topographic contrast remains constant. Vortices appear as light "cloud" like structures, while antidots appear as dark regions beneath the vortices.

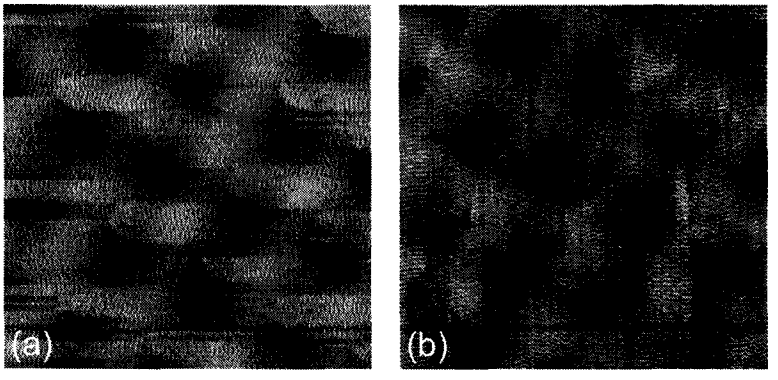

Figure 4.22: $3 \times 3\ \mu m^2$ area MFM images, acquired at 5.7 K, in a field of 62.1 G (H_3), of the exact same region. In (a), the tip scans from the left to the right, while in (b) the tip scans from the bottom to the top.

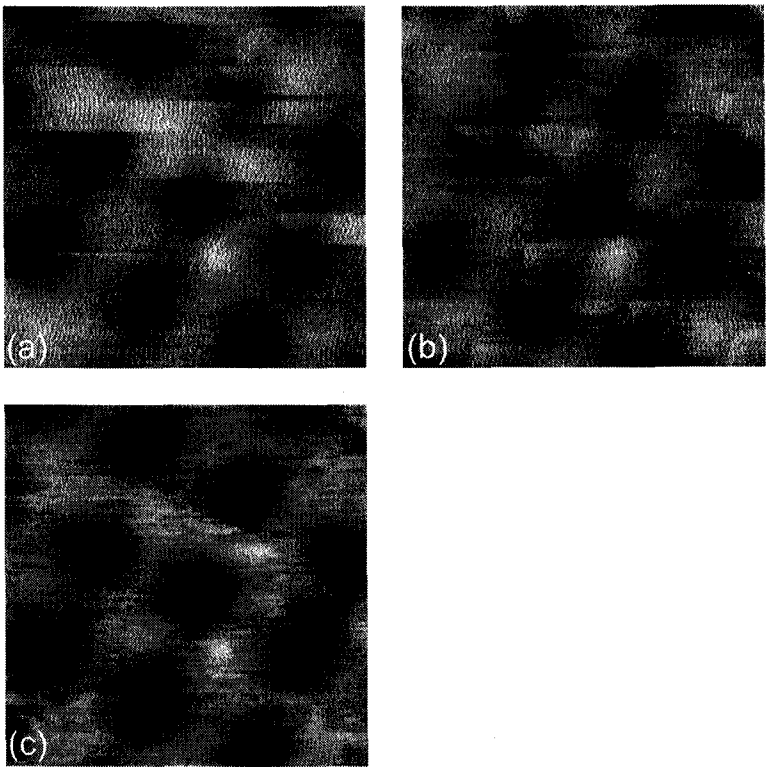

Figure 4.23: 2.5×2.5 μm^2 area MFM images, acquired at 5.7 K, in (a) 41.4 G (H_2), (b) 62.1 G (H_3), and (c) 82.8 G (H_4).

than one vortex. At small field strengths, vortices are preferentially resident only within the antidots (it is energetically favorable for vortices to reside within antidots as compared with interstitial site). They are then more difficult to image than their interstitial cousins, as their normal cores and magnetic fields are no longer confined within the respective characteristic lengths ξ and λ, but rather by the larger antidot diameter D. The increased spatial extent of their magnetic field results in a reduction of the magnetic field gradient, leading to a greatly diminished magnetic contrast. As the external magnetic field is increased to H_2 and beyond, antidots quickly become occupied and saturated. Additional vortices are then relegated to interstitial sites, where they may be more easily imaged.

Images as a function of height are shown in Fig. 4.24. We see that at larger scan heights little magnetic structure is evident. However, as the tip-sample separation is

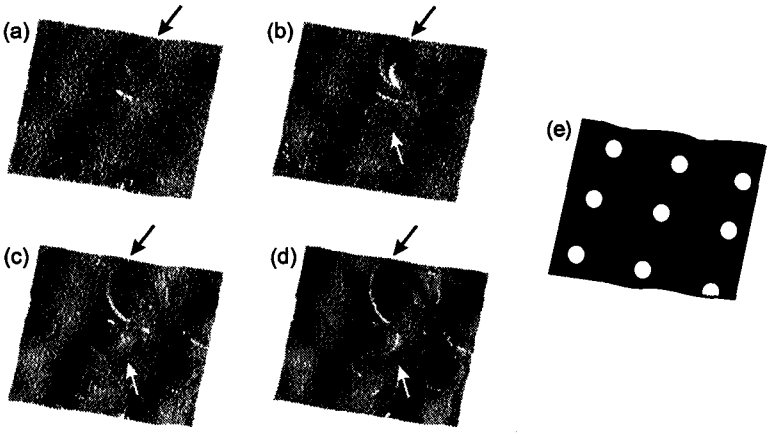

Figure 4.24: $2.5 \times 2.5\ \mu m^2$ area constant height MFM images, acquired at successively smaller tip-sample separations. The height interval between images is 75 nm, with (a) the farthest and (d) the closest to the sample surface. Panel (e) is a drawing of the region which reveals the position of the antidots. Images were acquired at 5.5 K in a field of 62.1 G (H_3). Tip induced movement of the vortices around the antidots is indicated by arrows. The data in these images have been specially processed in order to enhance contrast.

reduced, there appears to be increasing evidence of vortex motion around the antidots, the result of tip induced movement. Again, this is consistent with the fact that under these conditions of temperature and applied magnetic field, each antidot is saturated. Interstitial vortices, being forbidden to enter, instead are observed to circulate around the antidots.

In order to image the interstitial vortices more effectively with MFM, it is necessary to minimize the influence of the magnetic field of the tip on the vortices. This can be achieved either by reducing the tip magnetic moment, or alternatively by ensuring that interstitial vortices remain more securely pinned during the imaging process; this is effectively done by cooling the sample further.

With a reduction in temperature comes a corresponding increase in the saturation number of the antidots, as was shown in Fig. 4.3. This implies that in order to generate the required number of interstitial vortices, a larger external magnetic field must be applied. However, as was shown in Fig. 4.2, the most pronounced effects of the antidot lattice occur at smaller fields, with no observable enhancement of the critical current evident beyond the fourth matching field. Simply reducing the sample

temperature then would be an ineffective strategy. Instead, the solution lies with a change in size of the antidots, although it must be acknowledged that the production of large antidot arrays of suitable quality is not yet routine, given the complexity of the fabrication process. Samples with smaller antidots would saturate at lower fields and temperatures; for example, antidots with diameter $D \approx 133$ nm would saturate with one vortex at T = 5 K. This would produce an enhanced pinning effect for the vortices, thereby creating an environment more conducive to study by MFM.

5

Conclusion & Outlook

Low temperature magnetic force microscopy has been shown to be a versatile tool with which to study superconducting phenomenon. The technique offers the ability to probe materials on a local scale, and provides simultaneous magnetic and topographic contrast, both important features for the study of structured (patterned) samples. The ability to control and alter the sample environment, through changes in the temperature and applied magnetic field, permits operation under a broad range of working conditions, a feature which compliments well the technique's limited ability to study dynamic processes.

Measurements were performed using a custom built low temperature magnetic force microscope. During commissioning, the instrument was thoroughly characterized, a process which involved a careful consideration of the electronic and mechanical (i.e. cantilever) noise sources in the system. Emphasis was placed on maximizing the signal-to-noise ratio, a quantity directly related to the smallest measurable frequency shift.

Magnetic force spectroscopy data has been used to determine the critical temperature of superconducting samples. The technique exploits the temperature dependence of the repulsive interaction between the magnetic tip and the sample, a consequence of the Meissner effect. This mode of operation also shows promise as a means by which the magnetic penetration depth may be measured. It has been shown that an absolute quantitative determination of the penetration depth requires a comprehensive knowledge of the micromagnetic structure of the tip, although relative measurements

(e.g. changes in λ with temperature) may be possible irrespective of such details.

Images of vortices as a function of applied magnetic field demonstrated the expected linear relation between vortex density and field strength, confirming that only single vortices, each carrying one flux quantum, were imaged. It was observed that material pinning sites prevented the formation of a regular Abrikosov lattice, although short range hexagonal order was observed. Dissipation images of vortices suggested that the primary sources of energy loss include eddy current damping over the superconducting regions, and tip-induced vortex motion over the normal conducting cores. Studies as a function of temperature revealed that as pinning strengths decreased, a corresponding increase in the mobility of vortices was observed, reflected in larger hopping distances at higher temperatures.

A new method was presented for determining the magnetic penetration depth based upon the change in the observed vortex profile as a function of height above the sample surface. For the case of the unpatterned Nb film, the measured value was found to be within a factor of ~ 2.5 of the accepted value. A detailed knowledge of the tip structure was not required, although a more accurate result would be obtained by deconvolving the tip influence on the observed vortex profile. Nevertheless, the technique represents a useful alternative to the spectroscopy method when knowledge of the tip structure is limited.

Measurements of the patterned Nb film revealed that only interstitial vortices could be easily imaged, while vortices resident in antidots remained unobservable. However, at temperatures required to give the desired saturation number, magnetic contrast was poor, and interstitial vortices were too weakly pinned, resulting in significant tip induced motion of the vortices around the antidots at smaller tip-sample separations.

In regards to future work, the technique to determine the magnetic penetration depth based on magnetic force spectroscopy data is promising, and should be developed further. While achieving a detailed knowledge of the tip magnetic structure is challenging, it is possible in principle. Perhaps this, coupled with further development

of the theoretical treatment, will bring some advances.

It would also be worthwhile to examine in greater detail how to apply MFM towards the study of material pinning characteristics. A first step would perhaps be to compare existing data with new data acquired on the same sample after subjecting it to ion bombardment, a process which introduces additional material defects and thereby increases pinning.

Future studies of vortex interactions with antidot arrays by MFM will require an increase in pinning strengths in order to limit tip induced motion of vortices. This is realized, in effect, by working at lower temperatures, and necessitates a corresponding change in the antidot dimensions in order to achieve the desired saturation number, both of which are feasible. A concurrent quantitative study of the vortex field strength as a function of proximity to edges and other structures would also be interesting, to investigate whether non-integral values of the flux quantum can be observed by MFM.

BIBLIOGRAPHY

[1] http://www.superconductors.org

[2] Y. Martin and H. K. Wickramasinghe, Appl. Phys. Lett. **50**, 1455 (1987)

[3] P. Grütter, H. J. Mamin and D. Rugar, *Magnetic Force Microscopy*, Springer Ser. Surface Sciences, Vol. 28 (Springer, Berlin, Heidelberg 1992)

[4] A. Moser, H. J. Hug, B. Stiefel, and H.-J. Güntherodt, J. Magn. Magn. Mater. **190**, 114 (1998)

[5] C. W. Yuan, Z. Zheng, A. L. de Lozanne, M. Tortonese, D. A. Rudman, and J. N. Eckstein, J. Vac. Sci. Technol. B **14**, 1210 (1996)

[6] A. Volodin, K. Temst, C. Van Haesendonck, and Y. Bruynseraede, Physica C **332**, 156 (2000)

[7] G. P. Pepe, G. Ammendola, G. Peluso, A. Barone, L. Parlato, E. Esposito, R. Monaco, and N. E. Booth, Appl. Phys. Lett. **77**, 447 (2000)

[8] M. Roseman and P. Grütter, Rev. Sci. Instrum. **71**, 3782 (2000)

[9] G. Binnig, C. F. Quate, and Ch. Gerber, Phys. Rev. Lett. **56**, 930 (1986)

[10] U. Rabe, J. Turner, and W. Arnold, Appl. Phys. A: Mater. Sci. Process. **66**, S277 (1998)

[11] Dror Sarid, *Scanning Force Microscopy with Applications to Electric, Magnetic and Atomic Forces*, Oxford University Press, 1994

[12] B. Gotsmann, C. Seidel, B. Anczykowski, and H. Fuchs, Phys. Rev. B **60**, 11051 (1999)

[13] T. R. Albrecht, P. Grütter, D. Horne and D. Rugar, J. Appl. Phys. **69**, 668 (1991)

[14] F. J. Giessibl, Phys. Rev. B **56**, 16010 (1997)

[15] H. Hölscher, U. D. Schwarz, and R. Wiesendanger, Appl. Surf. Sci. **140**, 344 (1999)

[16] Manufactured by Samtec USA, New Albany, IN

[17] Epo-Tek H20E, manufactured by Epoxy Technology, Billerica, MA

[18] C. Julian Chen, *Introduction to Scanning Tunneling Microscopy*, Oxford University Press, 1993

[19] HS-J Geophone, manufactured by Geo Space Corporation, Houston, TX

[20] S. H. Pan, Piezo-electric motor, international patent publication No. WO93/19494, International Bureau, World Intellectual Property Organization (30 Sept. 1993)

[21] *Research Matters* (Oxford Instruments, Issue 9, Autumn 1998)

[22] http://www.thermomicroscopes.com

[23] http://www.nanosensors.com

[24] D. Rugar, H. J. Mamin and P. Güthner, Appl. Phys. Lett. **55**, 2588 (1989)

[25] R. E. Thomson, Rev. Sci. Instrum. **70**, 3369 (1999)

[26] C. W. Yuan, E. Batalla, M. Zacher, A. L. de Lozanne, M. D. Kirk, and M. Tortonese, Appl. Phys. Lett. **65**, 1308 (1994)

[27] M. A. Eriksson, R. G. Beck, M. Topinka, J. A. Katine, R. M. Westervelt, K. L. Chapman, and A. C. Gossard, Appl. Phys. Lett. **69**, 671 (1996)

[28] A. Volodin, K. Temst, C. Haesendonck, and Y. Bruynseraede, Appl. Phys. Lett. **73**, 1134 (1998)

[29] K. Petermann, IEEE J. Quantum Electron., **1**(2), 480 (1995)

[30] *LDX-3412 Instruction Manual,* ILX Lightwave, 1990

[31] *Optoelectronic Components Catalog,* UDT Sensors, Inc.

[32] *Photodiode Monitoring with Op Amps*, Burr Brown Application Bulletin AB-075, 1994

[33] Henry W. Ott, *Noise Reduction Techniques in Electronic Systems,* John Wiley & Sons, 1988

[34] W. Denk and D. W. Pohl, Appl. Phys. Lett. **59**, 2171 (1991)

[35] Y. Liu, Ph.D. thesis, McGill University, 1997

[36] U. Dürig, H. R. Steinauer, and N. Blanc, J. Appl. Phys. **82**, 3641 (1997)

[37] Timothy M. H. Wong, Ph.D. thesis, University of Cambridge, 1991

[38] K. Petermann, *Laser Diode Modulation and Noise*, Kluwer Academic Publishers, 1988

[39] G.P.Agrawal and N.K. Dutta, *Long-Wavelength Semiconductor Lasers*, Van Nostrand Reinhold, 1986

[40] Larry A. Coldren & Scott W. Corzine, *Diode Lasers and Photonic Integrated Circuits*, John Wiley & Sons Inc., 1995

[41] J. B. Johnson, Phys. Rev. **32**, 97 (1928)

[42] Mischa Schwartz, *Information Transmission, Modulation, and Noise*, McGraw-Hill Book Company, Inc., 1959

[43] *Feedback Plots Define Op Amp AC Performance*, Burr Brown Application Bulletin AB-028A, 1991

[44] A. C. Rose-Innes and E. H. Rhoderick, *Introduction to Superconductivity* (Pergamon Press, 1978) 2nd ed.

[45] M. Tinkham, *Introduction to Superconductivity* (McGraw-Hill, New York, 1996) 2nd ed.

[46] H. Kamerlingh Onnes, Leiden Comm. **122b**, 124 (1911)

[47] B. W. Roberts, J. Phys. Chem. Ref. Data **5**, 581 (1976)

[48] J. Nagamatsu, N. Nakagawa, T. Muranaka, Y. Zenitani, and J. Akimitsu, Nature **410**, 63 (2001)

[49] J. G. Bednorz and K. A. Müller, Z. Phys. **B64**, 189 (1986)

[50] W. Meissner and R. Ochsenfeld, Naturwissenschaften **21**, 787 (1933)

[51] F. London and H. London, Proc. Roy. Soc. **A149**, 71 (1935)

[52] C. J. Gorter and H. B. G. Casimir, Phys. Z. **35**, 963 (1934); Physica **1**, 306 (1934)

[53] E. A. Lynton, *Superconductivity* (Methuen, London 1962)

[54] H. Zhang, J. W. Lynn, C. F. Majkrzak, S. K. Satija, J. H. Kang and X. D. Wu, Phys. Rev. B **52**, 10395 (1995) and references therein

[55] J. E. Sonier, R. F. Kiefl, J. H. Brewer, D. A. Bonn, J. F. Carolan, K. H. Chow, P. Dosanjh, W. N. Hardy, R. Liang, W. A. MacFarlane, P. Mendels, G. D. Morris, T. M. Riseman, and J. W. Schneider, Phys. Rev. Lett. **72**, 744 (1994)

[56] P. G. de Gennes, *Superconductivity of Metals and Alloys*, (Addison-Wesley, New York, 1989)

[57] R. P. Huebener, *Magnetic Flux Structures in Superconductors*, (Springer-Verlag, Berlin, 2001)

[58] V. L. Ginzburg and L. D. Landau, Sov. Phys. JETP **20**, 1064 (1950)

[59] A. A. Abrikosov, Sov. Phys. JETP **5**, 1174 (1957)

[60] J. Bardeen, Phys. Rev. Lett. **7**, 162 (1961)

[61] A. L. Fetter, Phys. Rev. B **22**, 1200 (1980)

[62] V. G. Kogan, Phys. Rev. B **49**, 15874 (1994)

[63] A. K. Geim, S. V. Dubonos, I. V. Grigorieva, K. S. Novoselov, F. M. Peeters, and V. A. Scheigert, Nature **407**, 55 (2000)

[64] U. Essmann and H. Träuble, Phys. Lett. A **24**, 526 (1967)

[65] V. Metlushko, U. Welp, G. W. Crabtree, Zhao Zang, S. R. J. Brueck, B. Watkins, L. E. DeLong, B. Ilic, K. Chung, and P. J. Hesketh, Phys. Rev. B **59**, 603 (1999)

[66] M. Baert, V. V. Metlushko, R. Jonckheere, V. V. Moshchalkov, and Y. Bruynseraede, Phys. Rev. Lett. **74**, 3269 (1995)

[67] J. I. Martin, M. Velez, J. Nogues, and I. K. Schuller, Phys. Rev. Lett. **79**, 1929 (1997)

[68] A. T. Fiory, A. F. Hebard, and S. Somekh, Appl. Phys. Lett. **32**, 73 (1978)

[69] V. Metlushko, U. Welp, G. W. Crabtree, R. Osgood, S. D. Bader, L. E. DeLong, Zhao Zhang, S. R. J. Brueck. B. Ilic, K. Chung, and P. J. Hesketh, Phys. Rev. B **60**, 12585 (1999)

[70] A. Terentiev, B. Watkins, L. E. DeLong, L. D. Cooley, D. J. Morgan, and J. B. Ketterson, Physica C **332**, 5 (2000)

[71] V. V. Moshchalkov, M. Baert, V. V. Metlushko, E. Rosseel, M. J. Van Bael, K. Temst, R. Jonckheere, and Y. Bruynseraede, Phys. Rev. B **54**, 7385 (1996)

[72] D. J. Morgan and J. B. Ketterson, Phys. Rev. Lett. **80**, 3614 (1998)

[73] A. Bezryadin, Y. N. Ovchinnikov, and B. Pannetier, Phys. Rev. B **53**, 8553 (1996)

[74] G. S. Mkrtchyan and V. V. Schmidt, Sov. Phys. JETP **34**, 195 (1972)

[75] C. Reichhardt, C. J. Olson, and F. Nori, Phys. Rev. B **57**, 7937 (1998)

[76] A. Moser, H. J. Hug, O. Fritz, I. Parashikov, H.-J. Güntherodt, and T. Wolf, J. Vac. Sci. Technol. B **12**, 1586 (1994)

[77] M. W. Coffey, Phys. Rev. B. **57**, 11648 (1998)

[78] M. W. Coffey, Phys. Rev. Lett. **83**, 1648 (1999)

[79] A. Badía, Phys. Rev. B **60**, 10436 (1999)

[80] M. W. Coffey, J. Appl. Phys. **87**, 392 (2000)

[81] A. Badía, Phys. Rev. B **63**, 094502 (2001)

[82] C. T. Van Degrift, Rev. Sci. Instrum. **46**, 399 (1975)

[83] B. W. Langley, S. M. Anlage, R. F. W. Pease, and M. R. Beasley, Rev. Sci. Instrum. **62**, 1801 (1991)

[84] J. E. Sonier, J. H. Brewer, and R. F. Kiefl, Rev. Mod. Phys. **72**, 769 (2000)

[85] J. R. Kirtley, C. C. Tsuei, K. A. Moler, V. G. Kogan, J. R. Clem, and A. J. Turberfield, Appl. Phys. Lett. **74**, 4011 (1999)

[86] A. M. Chang, H. D. Hallen, L. Harriott, H. F. Hess, H. L. Kao, J. Kwo, R. E. Miller, R. Wolfe, and J. van der Ziel, Appl. Phys. Lett. **61**, 1974 (1992)

[87] S. J. Bending and A. Oral, J. Appl. Phys. **81**, 3721 (1997)

[88] http://math.nist.gov/oommf

[89] J. Lohau, S. Kirsch, A. Carl, G. Dumpich, and E. F. Wassermann, J. Appl. Phys. **86**, 3410 (1999)

[90] S. McVitie, R. P. Ferrier, J. Scott, G. S. White, and A. Gallagher, J. Appl. Phys. **89**, 3656 (2001)

[91] P. J. A. van Schendel, H. J. Hug, B. Stiefel, S. Martin, and H.-J. Güntherodt, J. Appl. Phys. **88**, 435 (2000)

[92] O. Fritz, M. Wülfert, H. J. Hug, H. Thomas, and H.-J. Güntherodt, Phys. Rev. B **47**, 384 (1993)

[93] M. W. Coffey and E. T. Phipps, Phys. Rev. B **53**, 389 (1996)

[94] G. Carneiro and E. H. Brandt, Phys. Rev. B **61**, 6370 (2000)

[95] V. Metlushko, private communication

[96] P. Grütter, Y. Liu, P. LeBlanc, and U. Dürig, Appl. Phys. Lett. **71**, 279 (1997)

[97] Y. Liu and P. Grütter, J. Appl. Phys. **83**, 7333 (1998)

[98] P. W. Anderson, Phys. Rev. Lett. **9**, 309 (1962); P. W. Anderson and Y. B. Kim, Rev. Mod. Phys. **36**, 39 (1964)

[99] A. Tonomura, H. Kasai, O. Kamimura, T. Matsuda, K. Harada, Y. Nakayama, J. Shimoyama, K. Kishio, T. Hanaguri, K. Kitazawa, M. Sasase, and S. Okayasu, Nature **412**, 620 (2001)

[100] D. Giller, A. Shaulov, T. Tamegai, and Y. Yeshurun, Phys. Rev. Lett. **84**, 3698 (2000)

[101] C.-H. Sow, K. Harada, A. Tonomura, G. Crabtree, and D. G. Grier, Phys. Rev. Lett. **80**, 2693 (1998)

[102] B. Pannetier, A. Bezryadin, and A. Eichenberger, Physica B **222**, 253 (1996)

[103] A. Bezryadin and B. Pannetier, J. Low Temp. Phys. **102**, 73 (1996)